THE UNIVERSITY of EDINBURGH

Edinburgh Research Explorer

A Mechanism of Cohesin-Dependent Loop Extrusion Organizes Zygotic Genome Architecture

Citation for published version:
Gassler, J, Brandao, HB, Imakaev, M, Flyamer, IM, Ladstatter, S, Bickmore, W, Peters, J-M, Mirny, LA & Tachibana, K 2017, 'A Mechanism of Cohesin-Dependent Loop Extrusion Organizes Zygotic Genome Architecture', *EMBO Journal*. https://doi.org/10.15252/embj.201798083

Digital Object Identifier (DOI):
10.15252/embj.201798083

Link:
Link to publication record in Edinburgh Research Explorer

Document Version:
Peer reviewed version

Published In:
EMBO Journal

General rights
Copyright for the publications made accessible via the Edinburgh Research Explorer is retained by the author(s) and / or other copyright owners and it is a condition of accessing these publications that users recognise and abide by the legal requirements associated with these rights.

Take down policy
The University of Edinburgh has made every reasonable effort to ensure that Edinburgh Research Explorer content complies with UK legislation. If you believe that the public display of this file breaches copyright please contact openaccess@ed.ac.uk providing details, and we will remove access to the work immediately and investigate your claim.

OPEN ACCESS

Download date: 05. May. 2023

A Mechanism of Cohesin-Dependent Loop Extrusion Organizes Zygotic Genome Architecture

Johanna Gassler,[1*] Hugo B. Brandão,[2*] Maxim Imakaev,[3,4] Ilya M. Flyamer,[5] Sabrina Ladstätter,[1] Wendy A. Bickmore,[5] Jan-Michael Peters,[6] Leonid A. Mirny,[2,3#] Kikuë Tachibana[1#]

[1]Institute of Molecular Biotechnology of the Austrian Academy of Sciences (IMBA), Vienna Biocenter (VBC), Dr. Bohr-Gasse 3, 1030 Vienna, Austria

[2]Harvard Graduate Program in Biophysics, Harvard University, Cambridge, Massachusetts 02138, USA

[3]Institute for Medical Engineering and Science, Massachusetts Institute of Technology (MIT), Cambridge, Massachusetts 02139, USA

[4]Department of Physics, MIT, Cambridge, Massachusetts 02139, USA

[5]MRC Human Genetics Unit, Institute of Genetics and Molecular Medicine (IGMM), University of Edinburgh, Edinburgh EH4 2XU, UK

[6]Institute of Molecular Pathology (IMP), VBC, Vienna Biocenter 1, 1030 Vienna, Austria

*These authors contributed equally to this work

[#]Corresponding authors: kikue.tachibana@imba.oeaw.ac.at; leonid@mit.edu

Character count (incl. spaces; excl. references): 75499

Running title: Loop extrusion organizes zygotic genomes

SUMMARY

Fertilization triggers assembly of higher-order chromatin structure from a condensed maternal and a naïve paternal genome to generate a totipotent embryo. Chromatin loops and domains have been detected in mouse zygotes by single-nucleus, (snHi-C) but not bulk, Hi-C. It is therefore unclear when and how embryonic chromatin conformations are assembled. Here, we investigated whether a mechanism of cohesin-dependent loop extrusion generates higher-order chromatin structures within the one-cell embryo. Using snHi-C of mouse knockout embryos, we demonstrate that the zygotic genome folds into loops and domains that critically depend on Scc1-cohesin and that are regulated in size and linear density by Wapl. Remarkably, we discovered distinct effects on maternal and paternal chromatin loop sizes, likely reflecting differences in loop extrusion dynamics and epigenetic reprogramming. Dynamic polymer models of chromosomes reproduce changes in snHi-C, suggesting a mechanism where cohesin locally compacts chromatin by active loop extrusion, whose processivity is controlled by Wapl. Our simulations and experimental data provide evidence that cohesin-dependent loop extrusion organizes mammalian genomes over multiple scales from the one-cell embryo onwards.

Keywords: chromatin structure/cohesin/loop extrusion/reprogramming/zygote

INTRODUCTION

Chromatin is assembled and reprogrammed to totipotency in the one-cell zygote that has the potential to generate a new organism. The chromatin template upon which higher-order structure is built in the embryo is different for the maternal and paternal genomes at the time of fertilization. The maternal genome is inherited from the meiosis II egg in which chromosomes are condensed in a mitotic-like state. In contrast, the paternal genome is contributed from compacted sperm chromatin that is extensively remodeled upon fertilization, as protamines are evicted and naïve nucleosomal chromatin is established (Rodman et al. 1981). The two genomes are reprogrammed as separate nuclei with distinct epigenetic signatures at the zygote stage (van der Heijden et al., 2005; Torres-Padilla et al, 2006; Mayer et al., 2000; Oswald et al., 2000; Ladstaetter and Tachibana-Konwalski, 2016). With the exception of imprinted loci, differences in chromatin states are presumably eventually equalized to facilitate the major zygotic genome activation (ZGA), which occurs at the 2-cell stage in mice (Aoki et al., 1997; Hamatani et al., 2004; Inoue et al., 2017). The establishment of zygotic genome architecture is therefore likely important for transcriptional onset and embryonic development.

Higher-order chromatin structures including chromatin loops, topologically associating domains (TADs) and compartmentalization of active and inactive chromatin, are established during embryonic development (Flyamer et al., 2017; Hug et al., 2017; Du et al., 2017; Ke et al., 2017). Using single-nucleus high resolution chromosome conformation capture (snHi-C), we previously identified the presence of loops and TADs in mouse zygotes (Flyamer et al., 2017) by averaging contact maps over the positions of annotated TADs and loops (Rao et al., 2014). In contrast, bulk Hi-C of mouse zygotes detected only weak or obscure domain structures that strengthened during preimplantation development (Du et al., 2017, Ke et al., 2017). However, it is not clear whether these bulk Hi-C approaches would detect the TADs and loops that are expected to form in interphase germinal vesicle-stage meiosis I oocytes (Flyamer et al., 2017). A combination of biological and technical factors, including smaller cell numbers used to analyze zygotes compared to blastocysts and different analyses of TAD aggregation data, may limit the detection of higher-order chromatin structures by bulk Hi-C (Du et al., 2017; Ke et al., 2017). Interestingly, TADs or loops are not detected in the rapidly dividing nuclei in early *Drosophila* embryos (Hug et al., 2017), or in metaphase II oocytes with condensed chromosomes (Du et al., 2017; Ke et al., 2017). Mitotic chromosomes in HeLa cells also lack TADs and loops, suggesting that this feature is not specific to meiosis II oocytes

(Naumova et al., 2013). Therefore, which higher-order chromatin structures are assembled in mammalian zygotes remains unresolved and the mechanisms that establish these structures in embryos are not known.

Studies in other cell types are beginning to provide insights into possible mechanisms that lead to the establishment of higher-order chromatin structures. An early stepping stone towards understanding chromatin structure was the unexpected finding that the cohesin complex, known to be essential for sister chromatid cohesion, is expressed in post-mitotic cells (Wendt et al., 2008). Cohesin is a tripartite ring consisting of Scc1-Smc3-Smc1. The cohesin ring is loaded onto chromatin by a loading complex composed of Nipbl/Scc2 and Mau2/Scc4 and is released from chromosomes by Wapl (Ciosk et al., 2000; Tedeschi et al, 2013; Gandhi et al, 2006; Kueng et al, 2006). Mutations in Nipbl cause Cornelia de Lange Syndrome (CdLS), which is characterized by gene expression defects and altered chromatin compaction but no obvious defects in sister chromatid cohesion (Deardorff et al., 2007; Krantz et al., 2004; Musio et al., 2006; Tonkin et al., 2004; Nolen et al., 2013). Therefore, the idea emerged that cohesin may have roles beyond holding sister chromatids together. The discovery that cohesin colocalizes with CTCF and mediates its transcriptional insulation led to the conceptual advance that cohesin may hold DNA together not only between sister chromosomes but also in *cis*, within chromatids (Wendt et al., 2008; Parelho et al., 2008). This is supported by the finding that depletion of Wapl leads to an increased residence time of chromosome-bound cohesin; moreover, it causes the formation of prophase-like chromosomes with cohesin-enriched axial structures termed “vermicelli” in G0 cells and affects chromosome condensation (Tedeschi et al., 2013; Lopez-Serra et al., 2013). This discovery suggested that cohesin organizes intra-chromatid loops in interphase.

Chromosome conformation capture (3C)-based methods described interphase TAD structures with cohesin and CTCF enrichment at the boundaries (Dixon et al., 2012; Nora et al., 2012; Rao et al., 2014; Vietri Rudan et al., 2015). These observations led to the testable prediction that cohesin is required for TAD formation. Cohesin depletion approaches including HRV protease-mediated cleavage, siRNA knockdown or conditional genetic knockout in cycling and differentiated cells had only minor effects on chromatin structure (Zuin et al.., 2013; Sofueva et al., 2013; Seitan et al., 2013), suggesting either that cohesin is not essential for TAD formation or protein depletion was inefficient. However, it was recently shown that auxin-inducible cohesin degradation leads to loss of TADs and loops in cancer cell lines (Rao et al., 2017; Wutz et al., 2017). Genetically knocking out the cohesin loading complex subunits Nipbl in post-mitotic liver cells and Mau2 in HAP1 cells also diminished the strength of TADs and loops (Schwarzer et al., 2017, Haarhuis et al., 2017).

A mechanism explaining the formation of TADs and loops is provided by the loop extrusion model. In this model (Fudenberg et al., 2016; Sanborn et al., 2015), dynamic chromatin loops are created in *cis* by loop extruding factors (LEFs). When a LEF binds to chromatin, it starts to translocate along the fiber in both directions, connecting successively further points, thus extruding a loop (**Figure 1A**). Translocation of loop extruders is hindered by boundary elements often located at TAD boundaries. Individual extruded loops are stochastic and can neither be visible in population Hi-C, nor distinguished from other contacts in snHi-C. Loop extrusion, however, leads to enrichment of contacts within TADs and recapitulates peaks of contact frequency commonly referred to as loops (**Figure 1B**). Cohesin is hypothesized to act as a loop extruder in interphase, while CTCF is likely the most prominent boundary element in mammalian cells (Fudenberg et al., 2016; Sanborn et al., 2015; Nora et al., 2017; Hansen et al., 2017).

Here we provide evidence that cohesin-dependent loop extrusion organizes higher-order chromatin structures of mammalian zygotic genomes. We show that cohesin is essential for chromatin loops and TADs but not compartments and other large-scale zygote-specific structures in one-cell embryos. We find that inactivating cohesin release by Wapl depletion exacerbates differences in

loop strengths between the maternal and paternal genomes that may be related to reprogramming. Remarkably, simulations indicate that most differences in global organization between the two zygotic genomes can be driven by changes in cohesin density and loop extrusion processivity. We further discovered that cohesin limits inter-chromosomal interactions by compacting chromatin; simulations indicate that this effect is due to altering the effective surface of chromosomes. We propose that cohesin-dependent loop extrusion organizes chromatin at multiple genomic scales from the mammalian one-cell embryo onwards.

RESULTS

Loops, TADs, and Compartments are Formed as Early as in One-Cell Embryos

Using snHi-C, we recently found that mouse zygotic genomes are organized into chromatin loops, TADs and compartments as early as G1 phase (Flyamer et al., 2017) (**Figure 2A**). However, bulk Hi-C of zygotes detected few or obscure TAD structures until around the 8-cell stage (Du et al., 2017; Ke et al., 2017). To attempt to resolve this conflict, we re-analyzed these recent data (Du et al., 2017; Ke et al., 2017).

Loop and TAD locations are generally conserved across cell types (Rao et al., 2014; Dixon et al., 2012) but are unknown in zygotes. Therefore to uncover higher-order chromatin organization in zygotes, we used a list of loop loci identified in CH-LX12 cells (Rao et al., 2014). For Hi-C data on low numbers of cells (Ulianov et al., 2017), loops and TADs are most visible when averaged over multiple positions (Flyamer et al., 2017) and normalized relative to control regions that are selected from random shifts of loop loci (**Appendix Figure S1A**). Using our approach, we found that these data support the presence of loops and TADs in 8-cell, 2-cell and even 1-cell embryos (**Figure 2B, Appendix Figure S1B**), and are in agreement with previous findings that TADs and loops become stronger with progressing development (Du et al., 2017, Ke et al., 2017). To exclude that these results are biased towards TADs called in CH-LX12 cells (Rao et al., 2014), we extended the analysis to include TADs called *de novo* in a variety of cell types including ES cells (Nora et al., 2017) (**Figure 2C**, **Figure EV 1**). We found that all *de novo* TAD calls, on over 15 data sets and multiple cell types, resulted in contact enrichments in all of the wild-type zygote data sets (**Figure 2C; Figure EV 1**) (this work, Flyamer et al. 2017, Du et al. 2017, Ke et al. 2017). Notably, contact enrichments were absent in metaphase II oocytes (Du et al., 2017), which, like mitotic cells, harbor condensed chromosomes (see **Figure 2A**) that presumably lack TADs (Naumova et al., 2013). Further, we discovered that zygotes lacking cohesin also do not form contact enrichments (see below).

In addition to this aggregate averaging analysis, we have visually identified certain genomic regions with TAD structures in heat maps of bulk Hi-C zygote data (**Figure EV 2**) (Du et al., 2017; Ke et al., 2017), suggesting that this organization can be detected independently of aggregate analysis. Together, these findings strongly support the folding of zygotic genomes into higher-order chromatin structures.

Zygotic Genome Architecture Changes During the First Cell Cycle

Higher-order zygotic chromatin structure is established *de novo* for paternal chromatin and re-established after chromosome decondensation for the maternal genome. We noted that loops differed in strength between the parental genomes in G1 phase, with stronger loops visible in paternal chromatin (**Figures 2B, D, E,** $p<0.05$, bootstrapping). It was conceivable that differences observed in G1 are transient and that loops, TADs and compartments change during the first cell cycle. To test this, we performed snHi-C of nuclei isolated from G2 phase zygotes (**Figure 2D**; see also **Table EV1 and EV2**). We found that zygotic genomes are organized into TADs, loops and compartments in G2 (**Figure 2D**), like in G1 phase. However, average loop and TAD strengths had

equalized between the genomes by G2 phase (**Figures 2B, 2D, 2E,** $p<0.05$, bootstrapping). To investigate the source of different G1 loop strengths, we classified loops into small (100-150 kb), intermediate (150-250 kb) and large (250-500 kb), and computed average loops for each distance. We found that paternal chromatin has higher contact frequency primarily for small length loops in G1 (**Appendix Figure S1C,** $p<0.05$, bootstrapping), which could be a consequence of loop formation following protamine-histone exchange on sperm chromatin.

Likewise, compartment strengths differ between the maternal and paternal genome in G1/S phase (**Figures 2B, D**), with maternal being much weaker and almost absent. In contrast with average loop and TAD strengths, a difference between maternal and paternal compartmentalization persisted through G2 (**Figure 2B** and **2D**) consistent with recent reports (Du et al., 2017; Ke et al., 2017). We thus conclude that initial differences in loop and TADs between zygotic maternal and paternal genomes become less evident by the end of the first cell cycle.

Cohesin is Essential for Zygotic Chromatin Folding into Loops and Domains

To gain insights into the mechanisms that generate zygotic genome architecture, we tested whether the candidate loop extruding factor cohesin is required for the formation or maintenance of loops and domains. We used a genetic knockout approach based on *(Tg)Zp3*-Cre, which conditionally deletes floxed alleles during the weeks of oocyte growth and generates maternal knockout zygotes after fertilization (**Figure 3A**). We have previously shown that Scc1 protein is efficiently depleted and sister chromatid cohesion fails to be established in $Scc1^{\Delta(m)/+(p)}$ zygotes (hereafter referred to as $Scc1^{\Delta}$ according to the maternal allele) (see **Figure EV 3B** and Ladstätter & Tachibana-Konwalski, 2016). Since sister chromatid cohesion is maintained by Rec8-cohesin in oocytes (Tachibana-Konwalski et al., 2010; Burkhardt et al., 2016), Scc1 depletion has no effect on chromosome segregation prior to fertilization and therefore a clean Scc1-cohesin knockout zygote is generated.

To test whether Scc1 is essential for TADs and loops in zygotes, we performed snHi-C (Flyamer *et al*, 2017) on genetically modified embryos. Both chromatin structures were detectable in control $Scc1^{fl}$ zygotes (**Figure 3B**). Remarkably, TADs and loops were largely, if not entirely, absent in $Scc1^{\Delta}$ zygotes, both in maternal and paternal nuclei (**Figure 3B**; **Figure EV 3C**). In contrast, compartmentalization of active and inactive chromatin from both maternal and paternal genomes was increased over 1.8-fold in $Scc1^{\Delta}$ compared to controls (**Figure EV 3C**). We conclude that cohesin is essential for loops and domains and antagonizes compartmentalisation, consistent with the notion that independent and possibly competing mechanisms generate these higher-order chromatin structures (Nora et al., 2017; Schwarzer et al., 2017; Haarhuis et al., 2017; Wutz et al., 2017; Nuebler et al., 2017).

Wapl Controls the Size of Cohesin-Dependent Chromatin Loops

The loss of loops and domains in the absence of cohesin could either be due to an indirect effect, for example on gene expression, or reflect a direct requirement for cohesin in loop formation. The loop extrusion model predicts that increasing the residence time of cohesin on chromosomes strengthens existing loops and promotes the formation of longer loops in a population of cells (Fudenberg et al., 2016). The residence time of cohesin on chromatin can be increased more than ten-fold by inactivating cohesin release through Wapl depletion (Tedeschi et al., 2013). To test whether TADs and loops in zygotes are enhanced by inactivating release of chromosomal cohesin, we generated $Wapl^{\Delta(m)/+(p)}$ *(*$Wapl^{\Delta}$*)* zygotes using the same strategy as described for *Scc1* (**Figure 3A**). The genetic deletion efficiency of *Wapl* is >98% (n=85 mice) (M. da Silva, J. M. Peters, personal communication), though we could not quantify the extent of protein depletion due to lack of Wapl antibodies that recognize the endogenous protein by immunofluorescence. We performed snHi-C of S/G2 phase $Wapl^{\Delta}$ zygotes and compared these to control data from $Wapl^{fl}$ zygotes, which are wild-type for

Wapl. Both TADs and loops were stronger in *Wapl*$^{\Delta}$ compared to control zygotes (**Figure 3B; Figure EV 3C;** see also **Appendix Table EV1** and **EV2**), in agreement with what has been observed in *Wapl*$^{\Delta}$ HAP1 and Wapl RNAi HeLa cells (Haarhuis et al. 2017; Wutz et al., 2017). Although formally we cannot exclude that these effects are due to changes in gene expression, the most parsimonious explanation for both loss of cohesin leading to loss of TADs and loops, and increase of cohesin residence time by Wapl depletion leading to stronger TADs and loops, is that the effect of cohesin is direct. Consistent with this, Nipbl depletion leads to loss of TADs and loops irrespective of changes in gene expression (Schwarzer et al., 2017). We conclude that cohesin release from chromosomes by Wapl is essential for regulating TADs and other local chromatin structures.

In addition to an effect on loops and TADs, we also observe that in the absence of Wapl, compartments became weaker than in controls by over 1.7-fold in both paternal and maternal genomes (**Figure 3A**; **Figure EV 3C**). These observations lend further support to the idea that cohesin antagonizes compartmentalisation and are consistent with data and simulations in recent work (Haarhuis et al., 2017; Nuebler et al., 2017).

We next tested whether inactivating cohesin release from chromosomes causes changes to average strengths of loops. We found that loops are stronger in pooled *Wapl*$^{\Delta}$ zygote data compared to controls for all tested genomic distances (**Figure 3C** and **3D,** $p<0.05$ by bootstrapping). Interestingly, unlike for controls in which loop strength was invariant with increasing distance, *Wapl*$^{\Delta}$ zygotes displayed increasing loop strength from short to large distances with up to 80% enrichment of contacts above background levels (**Figure 3D**). These results are consistent with the loop extrusion mechanism and suggest that in wild-type cells, Wapl limits the extent of loop extrusion by releasing cohesin from chromosomes, impeding the amount of chromatin-associated cohesin and its processivity. Altogether, we conclude that cohesin directly regulates loop and domain formation or maintenance in the one-cell embryo.

Cohesin organizes chromosomes at the sub-Megabase scale

To further investigate how cohesin shapes genome architecture, we studied the genome-wide contact probability, $P_c(s)$, for chromatin loci separated by genomic distances, s. Consistent with our previous observations of wild-type zygotes (Flyamer et al., 2017), control cells have a $P_c(s)$ curve that changes slowly below 1 Mb, reflecting local chromatin compaction; it changes steeply at or after 1 Mb in both maternal and paternal chromatin and exhibits another plateau near 10 Mb in maternal chromatin, likely reflecting long-range chromatin interactions remaining from compaction to the mitotic state (**Figure 4A; Appendix Figure S2;** see also **Appendix Figure EV1 and EV2**) (Flyamer et al., 2017; Naumova et al., 2013). Interestingly, the $P_c(s)$ curve of *Scc1*$^{\Delta}$ zygotes lost the shallow <1 Mb region, and followed a power law of $s^{-1.5}$, up to 1 Mb in both maternal and paternal genomes; the power law stretched up to 10 Mb in paternal chromatin (**Figure 4B; Appendix Figure S2**). This indicates that in the absence of cohesin, zygotic chromatin resembles a three-dimensional random walk as previously observed in yeast (Tjong et al., 2012; Mizuguchi et al., 2014; Halverson et al., 2014). Conversely, in *Wapl*$^{\Delta}$ zygotes, the contact probability was enriched and more shallow up to ~300 kb further than in controls (**Figure 4C**). Contact probability features at >10 Mb remain largely unchanged in both *Scc1*$^{\Delta}$ and *Wapl*$^{\Delta}$ $P_c(s)$ curves. Therefore, differences in long-range interactions (>10 Mb) between maternal and paternal chromatin are cohesin-independent. Thus, we conclude that cohesin is directly involved in shaping the $P_c(s)$ curve up to ~1 Mb, and its effect is a deviation in contact probability above the $s^{-1.5}$ power-law in mouse zygotic chromatin.

Average extruded loop sizes can be derived from $P_c(s)$ curves and simulations

To help elucidate the mechanism of loop formation by cohesin, we developed a new method for analysis of $P_c(s)$ curves aiming to derive sizes of extruded loops and linear density of cohesin. We

developed and tested this method using polymer simulations of loop extrusion, where sizes of loops and linear density of extruders are either set or can be directly measured. Our analysis shows that average loop sizes and cohesin density can be found by studying the derivative of the $P_c(s)$ curve in log-log space i.e. the slope of $log(P_c(s))$ (**Figure EV 4A**): The location of the maximum of the derivative curve (i.e. position of the smallest slope) closely matches the average length of extruded loops, and the depth of the local minimum at higher values of *s* increases with the linear density of loop-extruding cohesin in simulated chromatin (**Figure EV 4A**). Note that sizes of extruded loops are smaller than the processivity of each cohesin, defined as the loop size extruded by unobstructed cohesin, suggesting some degree of crowding of cohesins on DNA (**Appendix Figure S3**), as expected theoretically (Fudenberg et al., 2016; Goloborodko et al., 2016) and illustrated schematically (**Figure 1**). We validate this approach, using recent population Hi-C data for *Wapl*$^{\Delta}$ and control HAP1 cells (Haarhuis et al., 2017) (**Figure EV 4B**). We demonstrate that a two-fold increase in cohesin density in *Wapl*$^{\Delta}$ can be inferred from the $P_c(s)$ curves, which matches experimentally measured values (**Figure EV 4A-B**) (see Figure 4E in Haarhuis et al., 2017); moreover, we infer that the average size of an extruded cohesin loop in the HAP1 cells is ~120 kb in controls and ~300 kb in the *Wapl*$^{\Delta}$ condition.

We note that the extruded loops with the average size <300 kb are different from peaks of Hi-C contact frequency, also referred as "loops", that are typically formed by CTCF-rich TAD boundaries located up to 1 Mb from each other. Such peaks of interactions between boundaries also arise in simulations; they rarely represent a single boundary-to-boundary loop, and are typically formed by a collection of much smaller cohesin extruded loops that have bumped into each other and have stopped at TAD boundaries (**Figure 1A**). Due to the stochastic nature of cohesin loading and extrusion, the location of individual extruded loops formed by stalled cohesin varies from cell to cell and is not visible as an enrichment in Hi-C maps (**Figure 1B**). These loops, however, bring two boundaries closer to each other, and since boundary locations are set genomically, enrichment on interactions between boundaries become visible as peaks in Hi-C maps (referred here as "Hi-C loops"). In all, this new method for analysis of $P_c(s)$ curves provides a framework for the interpretation of genome-wide contact probability and is complementary to identification of contact frequency peaks ("Hi-C loops") visible in Hi-C maps.

Loop extrusion leads to differences in compaction of maternal and paternal chromatin

Interpreting our zygote data using the $P_c(s)$ curve analysis, we estimated that loop extrusion by cohesin results in an average extruded loop size of 60-70 kb in control G1 zygotes (**Figure 4A**). In contrast, in *Wapl*$^{\Delta}$ zygotes, the length of loops extruded by cohesin was doubled to 120 kb whereas no loops could be detected in Scc1$^{\Delta}$ zygote data (**Figure 4B, C**). As a complementary approach, we performed polymer simulations at a range of cohesin density and processivity parameters and found values that provide the best agreement between simulations and experimental data, as measured by agreement of the $P_c(s)$ curves (**Figures 4D-F**): We obtain 74 kb as the average size of extruded loops for control zygotes (both maternal and paternal), 111 kb for paternal *Wapl*$^{\Delta}$ and 165 kb for maternal *Wapl*$^{\Delta}$ zygotic chromatin. In addition, the best-matching models provide estimates for the processivity and linear density of cohesin in these cells: for control zygotes we obtain a processivity of 120 kb and density of one cohesin per 120 kb (assuming one cohesin per loop extrusion complex). For *Wapl*$^{\Delta}$ zygotes, we require a much higher processivity of 480 kb in both maternal and paternal zygotes, and a linear density of one cohesin per 120 kb in maternal and 60 kb in paternal chromosomes. We conclude that Wapl is mostly regulating cohesin processivity, as linear density may be limited by the available number of cohesin complexes per nucleus.

To examine how Hi-C loops differ between the Wapl maternal and paternal genomes, we quantified their strength (**Appendix Figure S1C**) as done in **Figures 2** and **3**. We found that Hi-C loop strengths generally increased in the case of both maternal and paternal genomes. Analyzing the insulation in *Wapl*$^{\Delta}$ zygotes (see **Materials and Methods**) also showed stronger insulation at TAD/loop borders in

paternal chromatin (**Figure EV 3D)**. The stronger Hi-C loops, stronger insulation, and higher cohesin density may all result from higher cohesin loading rate and reflect the transcriptionally permissive state specific for paternal chromatin (Adenot et al., 1997), suggesting that higher transcription leads to loading of additional cohesins, whose effects are exacerbated in *Wapl*$^{\Delta}$ where cohesin unloading is suppressed. This also suggests that transcription is not required for loop extrusion *per se*, as the maternal genome is thought to be transcriptionally inactive.

Next, we used microscopy to test whether these differences in loops between maternal and paternal chromatin lead to changes in chromatin compaction in *Wapl*$^{\Delta}$ zygotes. To monitor chromatin compaction, we expressed Scc1-EGFP in *Wapl*$^{\Delta/\Delta}$ and *Wapl*$^{fl/fl}$ oocytes, performed *in vitro* fertilization and imaged zygotes by time-lapse microscopy (**Appendix Figure S4A**). Chromatin in *Wapl*$^{\Delta}$ zygotes is expected to form "vermicelli", prophase-like chromosomes with cohesin-enriched axial structures that can be detected by visualization of Scc1 (Tedeschi et al., 2013; Lopez-Serra et al., 2013). Scc1-EGFP formed a uniform diffuse pattern in the nuclei of control zygotes (**Appendix Figure S4B**). In contrast, Scc1-EGFP showed a non-homogeneous distribution in maternal and paternal nuclei of *Wapl*$^{\Delta}$ zygotes (**Appendix Figure S4C**). This distribution might reflect vermicelli that are obscured due to the presence of endogenous Scc1 within cohesin complexes, leading to a high background of free Scc1-EGFP. To ensure that all cohesin contains Scc1-EGFP, we expressed Scc1-EGFP in *Scc1*$^{\Delta/\Delta}$*Wapl*$^{\Delta/\Delta}$ oocytes (**Figure 5A-C; Movie EV1 and EV2; Appendix Figure S5A** and **S5B**). Indeed, this approach increased the detection of vermicelli as worm-like structures in both nuclei of *Scc1*$^{\Delta}$*Wapl*$^{\Delta}$ zygotes (**Figure 5B** and **5C; Movie EV2; Appendix Figure S5C**). Vermicelli-like structures were especially evident in maternal nuclei in both *Wapl*$^{\Delta}$ and *Scc1*$^{\Delta}$*Wapl*$^{\Delta}$ zygotes. Vermicelli formation occurs prior to the major ZGA (Aoki et al., 1997; Hamatani et al., 2004), consistent with the idea that transcription is not essential for Hi-C loop formation (Du et al., 2017, Ke et al., 2017). We conclude that inactivation of cohesin release leads to vermicelli formation in maternal and paternal zygotic chromatin.

To quantify maternal and paternal chromatin compaction, we examined DNA morphology at higher resolution in fixed zygotes. Both maternal and paternal chromatin is compacted into vermicelli-like structures and is revealed most clearly in individual z-sections of *Wapl*$^{\Delta}$ zygotes (**Figure 6A** and **6B**). We observed a significant change in the coefficient of variation in intensity between control and *Wapl*$^{\Delta}$ zygotes (**Figure 6C; Appendix Figure S6;** p-value=$1.88*10^{-7}$). Additional DAPI-intense structures surrounding the pre-nucleolar regions were visible specifically in maximum intensity projections in the maternal nucleus (n=25/33 zygotes, **Figure 6A** and **6B**), indicating a higher degree of compaction in maternal than paternal chromatin. These DAPI-intense structures likely correspond to the more prominent vermicelli observed in maternal nuclei in time-lapse movies (**Figure 5B** and **5C; Appendix Figure S4C; Movie EV2**). Quantification of the texture in images using the grey-level co-occurrence matrices revealed that the contrast between pixels is stronger in maternal than paternal nuclei (**Figure 6D** and **Appendix Figure S7** and **S8**), implying a more structured and less homogeneous nuclear architecture. To study the DAPI-intense structures, we performed additional segmentation analysis and compared the size distributions of identified objects between conditions and nuclei. The size of DAPI-intense structures significantly increased in *Wapl*$^{\Delta}$ zygotes (p-values $1.25*10^{-11}$ and $8.23*10^{-28}$ for maternal and paternal nuclei, respectively (**Figure 6E**). Maternal nuclei contain slightly bigger objects than paternal nuclei (p-value 0.00014), which might reflect stronger vermicelli. We suggest that inactivating cohesin release has a differential effect on chromatin compaction of maternal and paternal chromatin.

To corroborate the major reorganization observed by microscopy and snHi-C in *Wapl*$^{\Delta}$ zygotes, we examined our polymer simulations of *Wapl*$^{\Delta}$ conditions to see whether the 3D organization of cohesins in modeled conformations displayed preferentially "axially enriched" structures (**Appendix Figure S3**). We found consistently that vermicelli are visible in the paternal *Wapl*$^{\Delta}$ chromatin simulation, but are not visible in controls (**Figure 4G** and **4I**); at odds with expectations, maternal

chromatin formed weaker vermicelli (**Figure EV 4C; Appendix Figure S3**). This result suggests that some other processes beyond loop extrusion may contribute to formation of vermicelli in maternal zygotes. Nevertheless, both our snHi-C data and microscopy show that loop formation differs for zygotic maternal and paternal genomes when cohesin release is prevented by Wapl depletion. By regulating cohesin release, Wapl thus maintains interphase chromatin in a less compact state; moreover, it restricts the size of extruded cohesin loops and density of chromatin-associated cohesin.

Cohesin loop extrusion limits inter-chromosomal interactions

Population and single-cell Hi-C studies have revealed that interactions between non-sister chromatids (*trans*-contacts) are diminished during mitosis (Naumova et al., 2013; Nagano et al., 2017). A possible interpretation is that a more compact, linearly ordered chromosome directly affects the frequency of inter-chromosomal interactions. To investigate whether vermicelli chromosomes are more mitotic-like, and to test whether cohesin might play a role in chromosome compaction, we quantified the levels of *trans*-contacts, in zygotic chromatin by snHi-C (**Figure 7A;** see **Materials and Methods; Table EV1** and **EV2**). We found inter-chromosomal contact frequencies of 8% for nuclei in interphase (G1/S or G2), consistent with values reported for mouse ES cells at a similar cell cycle stage (Nagano et al., 2017). Interestingly, $Wapl^{\Delta}$ zygotes had reduced *trans* interaction fractions, with a mean value of 6% for paternal zygotic chromatin that is closer to values reported for early G1 (Nagano et al., 2017) but not significantly different from controls ($p<0.2$, Mann-Whitney U-test). In contrast, $Scc1^{\Delta}$ cells showed significantly larger *trans* interaction fractions as compared to controls (**Figure 7A**; an over 40% increase, $p<0.02$ Mann-Whitney U-test). These results suggest a possible novel role for chromosomal Scc1-cohesin in reducing interaction frequencies between non-sister chromatids.

To investigate the mechanism by which cohesin modulates inter-chromosomal interactions, we turned to polymer simulations of loop extrusion. We tested how varying cohesin processivity and linear density affected absolute numbers of contacts within and between chromosomes (**Appendix Figure S9A**). We found that an increase in processivity or density of cohesins resulted in an increase in intra-chromosomal contacts and a decrease in the absolute and relative *trans*-chromosomal contacts (**Appendix Figure S9A**). Thus, simulations suggest that cohesin can regulate frequencies of contacts between chromosomes.

To better understand how loop extrusion that operates at the sub-megabase scale can affect inter-chromosomal contacts, we examined the effects of loop extrusion on the sizes of chromosomes and shapes of their surfaces (**Figure 7B; Figure 8A**). We varied cohesin processivity and linear density and measured their effects on the simulated chromatin volume and surface area defined from the polygon that covers the modeled chromosomes (concave hull) (see **Materials and Methods**). We found that an increase in processivity and linear density of cohesins from $Scc1^{\Delta}$ to control to $Wapl^{\Delta}$ levels led to a gradual decrease in the number of *trans* interactions, a decrease in volume and a decrease in surface area (**Figure 7B; Figure 8B**); this trend was not sensitive to the choice of simulated Hi-C capture radius, or chromosome monomer radius for the convex hull measurement (**Appendix Figure S9B**). Interestingly, we found that the chromosome surface area was a good predictor of the fraction of inter-chromosomal interactions changing over 80% almost linearly from the simulated $Wapl^{\Delta}$ to $Scc1^{\Delta}$ conditions; however, whereas volume was predictive, it changed by only 40% and was nonlinear (**Figure 7B; Appendix Figure S9B**).

By visualizing polymer conformations for low and high cohesin densities, we found that a decrease in the number of extruded loops lead to a surface roughening, whereas increased compaction by loop extrusion smoothened out the polymer surface, resulting in fewer inter-chromosomal contacts (**Figure 7C**; **Figure 8A**). These simulations demonstrate that loop extrusion operating at <1 Mb scale

can affect long-range interactions by modulating the surface area of chromosomes, leading to changes in inter-chromosomal interaction frequencies. Super-resolution microscopy of continuously stained chromosomal regions may be able to observe the predicted roughening of chromosomal surfaces upon loss of cohesin.

DISCUSSION

Our data supports a direct role of cohesin in the formation or maintenance of chromatin loops and TADs. Cohesin was identified over two decades ago for its role in chromosome segregation, sister chromatid cohesion, and DNA damage repair (Peters et al., 2008). More recent studies have shown that cohesin colocalizes with CTCF and is associated with TADs and chromatin loops (Wendt et al., 2008; Dixon et al., 2012; Nora et al., 2012; Phillips-Cremins et al., 2013; Rao et al., 2014), which implicated cohesin as a regulator of intra-chromosomal structure. Since chromatin loops and TADs may have functional roles in gene regulation, such as preventing aberrant expression of genes (Lupianez et al., 2015; Franke et al., 2016; Flavahan et al., 2015), it has become a major endeavour to understand to what degree cohesin is involved in shaping chromatin structure. Early studies directly degrading or knocking out cohesin showed only mild effects on chromatin structure (Seitan et al., 2013; Sofueva et al., 2013; Zuin et al., 2014).

We show that genetic deletion of the Scc1 subunit of cohesin in mouse oocytes abolishes formation or maintenance of loops and TADs in the one-cell embryo. In contrast, chromatin loops are larger on average when cohesin release from chromosomes is prevented by Wapl depletion. Together, these results demonstrate that cohesin is essential for loops and TADs, and show that cohesin directly regulates their structure, consistent with recent studies that were published while this paper was under review. A recent study in a human cancer cell line (Rao et al., 2017) shows loss of loops and TADs upon acute degradation of Scc1/Rad21; similar results using this approach in HeLa cells were obtained in a recent pre-print (Wutz et al., 2017). Another study of a HAP1 human cell line (Haarhuis et al., 2017) demonstrates that *Wapl* deletion leads to higher density of cohesin on DNA and increases contact frequency of distant Hi-C loops. Finally, a recently published study achieved depletion of chromatin-associated cohesin by deletion of *Nipbl* in post-mitotic liver cells, which led to disappearance of loops and TADs (Schwarzer et al. 2017).

We extend these studies by uniquely obtaining both a decrease and an increase of cohesin, relative to the wild type, in the same biological system. This allowed us to gain insights into the fundamental principles of chromatin organization, developing a single polymer model that was able to reproduce chromosomal phenotypes at all three conditions, providing quantitative estimates of characteristics of cohesin-mediated loop extrusion, and making predictions about the effect of loop extrusion on long-range interactions by roughening of chromosomal surfaces. Our work also diverges from these reports in that we show cohesin is essential for forming loops and TADs starting from the one-cell embryo, which was hitherto unclear.

Crucially, our system enabled us to study how cohesin differentially affects the establishment of higher-order structure in maternal and paternal genomes that undergo reprogramming to totipotency. Interestingly, differences in maternal and paternal chromatin loops became more evident in $Wapl^{\Delta}$ zygotes. As in controls, paternal chromatin loops were stronger, and TADs more insulating than in maternal chromatin. Unlike controls, loop sizes differed by an estimated 60 kb, with longer loops present in the maternal genome. By microscopy, we also observed differences in global chromatin compaction between maternal and paternal genomes in $Wapl^{\Delta}$ zygotes. We speculate that the differences are due to a combination of distinct epigenetic modifications and loop extrusion dynamics.

Our data strongly support a model that cohesin forms loops and TADs by the mechanism of active loop extrusion (Fudenberg et al., 2016; Sanborn et al., 2015), and provides a quantitative rationale for the longer loop lengths in the *Wapl*$^{\Delta}$ zygotes. Our polymer simulations suggest that the key determinants for global genome organization by cohesins are their density and processivity, which is the product of residence time and extrusion velocity. Longer chromatin loop sizes in *Wapl*$^{\Delta}$ zygotes are quantitatively consistent with about a four-fold increase in cohesin processivity in the absence of Wapl, which results in about a 50% increase in the sizes of extruded loops as estimated from the derivative of $\log(P_c(s))$. Our present data do not distinguish whether increase in processivity reflects an increase in loop extruding speed, residence-time or both, but this is an interesting avenue for future research. Interestingly, sizes of extruded loops are smaller than processivity since extrusion is obstructed by interactions of boundary elements (with CTCF among them) and other chromatin-associated cohesins. In support of the model of active loop extrusion, Wang and coworkers recently provided the first direct *in vivo* evidence that condensins, which are related to cohesins, actively translocate on bacterial chromatin and align flanking chromosomal DNA (Wang et. al, 2017; Tran et al., 2017). A recent *in vitro* study has since demonstrated that eukaryotic yeast condensins are mechanochemical motors that translocate along DNA in an ATP-dependent fashion (Terekawa et al., 2017). Thus, it is likely that eukaryotic cohesins employ active loop extrusion to form chromatin loops and TADs, but we cannot rule out the possibility that accessory factors aid the extrusion process.

In contrast with our findings, two recent reports of the higher-order chromatin organization in mammalian embryos suggested that the mammalian zygote genome is largely unstructured (Du et al., 2017; Ke et al., 2017). In both studies, no or obscure TADs were detected in embryos before the 8-cell stage (Du et al., 2017; Ke et al., 2017), where TADs were detected using insulation scores and directionality index analysis (Dixon et al., 2012; Giorgetti et al., 2016) with a large window size (0.5-1 Mb). We note that non-zero insulation scores or directionality indices do not necessarily reflect the existence of a TAD since these metrics cannot distinguish TADs from compartments without other information; weak compartments in zygotes can further affect insulation scores or directionality indices. To further investigate whether TADs and loops exist in zygotes, we re-analyzed data from these studies. Using known positions of TADs and loops, we identified TADs and loops at all embryonic development stages. To exclude biases introduced by TAD positions used in the analysis, we tested TADs identified in many diverse cell types as well as TADs called *de novo* in bulk Hi-C of inner cell mass cells of blastocyst embryos (Du et al., 2017). Our ability to detect TADs in re-analyses of bulk Hi-C studies (Du et al., 2017, Ke et al., 2017) can be attributed to the higher statistical power of methods that we employed: not only did we aggregate TADs from positions called in population Hi-C data, but we also used observed-over-expected maps to correct for $P_c(s)$ specific for the used Hi-C map and rescaled TADs of different sizes (100 kb-1 Mb), allowing to depict the structure of the TAD body independently of TAD sizes upon averaging. The lack of rescaling of TADs (as well as different normalization) in the original analysis could have lead to blurring of signal in aggregate analysis. We further validated our method by visual inspection of Hi-C maps that showed both regions lacking contact enrichment and other regions containing domain structures. We furthermore show that the structures detected by aggregate analysis depend critically on cohesin, which is in line with its proposed role in loop and TAD formation.

Loops and TADs are weaker in zygotes than for later stage embryos, consistent with previous reports (Du et al., 2017; Ke et al., 2017). There are several possible explanations for this phenomenon, such as weaker or fewer boundary elements, lower rate of cohesin loading, or lower cohesin processivity. The difference in processivity is unlikely as our analysis suggests a similar processivity in paternal zygotic chromatin and HAP1 cells. On the other hand, we show both TAD and loop strengths are greater in the early G1 paternal zygotic genome, but these differences disappear in G2 as both genomes approach the major ZGA. We thus suggest that the weaker structural features seen in the

zygotic genome arise due to either paucity of boundary elements for cohesin loop extrusion or lower amounts of chromatin-associated cohesin.

Unexpectedly, we discovered that cohesin-dependent chromosome compaction reduces inter-chromosomal interactions in interphase. We therefore propose a model in which the surface roughness of chromosomes affects inter-chromosomal interactions and absence of cohesin leads to more interdigitation between chromosomes. We speculate as to what might be the functional consequences of increased inter-chromosomal interactions due to interphase chromosome decompaction. Given that topoisomerases cannot distinguish between DNA strands in *cis* and in *trans*, it is conceivable that increased number of *trans* interactions could lead to catenations that can be damaging during chromosome segregation. We therefore propose that the ancestral role of cohesin in forming intra-chromosomal loops during interphase could help promote proper chromosome segregation during cell division.

Our model of cohesin as a chromatin surface area regulator also raises important new points. If the active formation of loops can reduce inter-chromosomal interactions, then it is conceivable that loop formation creates local neighbourhoods on the chromatin fiber that also reduce the frequency of interactions with more distal segments of chromatin on the same chromosome. We speculate that the formation of loops can have important implications for reducing spurious enhancer-promoter looping interactions by reducing interdigitation between distant regions of the same chromosome.

In all, our work establishes which higher-order chromatin structures are built shortly after fertilization in the mammalian zygote. The differences in maternal and paternal loops generated by cohesin-dependent loop extrusion provide an entry point to understanding how the two genomes change from a transcriptionally silent and terminally differentiated state to a transcriptionally active and totipotent embryonic state.

MATERIALS AND METHODS

Mice

The care and use of the mice were carried out in agreement with the authorizing committee according to the Austrian Animal Welfare law and the guidelines of the International guiding principles for biomedical research involving animals (CIOMS, the Council for International Organizations of Medical Sciences). Mice were kept at a daily cycle of 14 hours light and 10 hours dark with access to food *ad libitum*. All mice were bred in the IMBA animal facility. *Scc1*$^{fl/fl}$ mice were bred on a mixed background (B6, 129, Sv). *Wapl*$^{fl/fl}$ mice were bred on a primarily C57BL/6J background. *Scc1*$^{fl/fl}$ *Wapl*$^{fl/fl}$ mice were bred on the same mixed background as Scc1$^{fl/fl}$ mice. Experimental mice were obtained by mating of homozygous floxed females to homozygous floxed males carrying *Tg(Zp3-Cre)* (Lewandoski *et al*, 1997; Lan *et al*, 2004). To obtain zygotes B6CBAF1 stud males were mated to *Scc1*$^{fl/fl}$ *Tg(Zp3-Cre)*, while C57BL/6J stud males were used for mating *Wapl*$^{fl/fl}$ *Tg(Zp3-Cre)* females. Sperm for *in vitro* fertilization of *Scc1*$^{fl/fl}$ *Wapl*$^{fl/fl}$ *Tg(Zp3-Cre*) oocytes was obtained from B6CBAF1 stud males.

No statistical methods were used to estimate sample size. No randomization or blinding was used.

Zygote collection

To obtain zygotes 3-5 week old female mice were superovulated by intraperitoneal injection of PMSG (pregnant mare's serum gonadotropin; 5 IU, Folligon, Intervet or 5 IU, Prospecbio) followed by hCG (human chorionic gonadotropin; 5 IU, Chorulon, Intervet) injection 48 hours later. Females were mated to wildtype stud males overnight. The following morning zygotes were released from the ampullae and treated with hyaluronidase to remove cumulus cells.

Single-nucleus Hi-C

Single-nucleus Hi-C was carried out as described before (Flyamer et al., 2017). After pronuclear extraction *Scc1*$^{fl/fl}$ *Tg(Zp3-Cre)* pronuclei used in the experiments were fixed around 19-22 hours post hCG injection (corresponding to about 7-10 hours post fertilization) and therefore are expected to be in G1/S-phase of the cell cycle. *Wapl*$^{fl/fl}$ *Tg(Zp3-Cre)* were fixed later around 23-27.5 hours post hCG injection (corresponding to about 11-15.5 hours post fertilization) and are expected to be in S/G2 phase of the cell cycle. To obtain G2 phase data zygotes were fixed 27 hours post hCG injection (corresponding to about 15 hours post fertilization) and lysed, pronuclei were separated into different wells after SDS lysis according to their size. No blinding or randomization were used for handling of the cells.

Briefly, after pronuclei were isolated, they were fixed in 2% formaldehyde for 15 minutes, then lysed on ice in lysis buffer (10 mM Tris-HCl pH 8.0, 10 mM NaCl, 0.5% (v/v) NP-40 substitute (Sigma), 1% (v/v) Triton X-100 (Sigma), 1× Halt^{TM} Protease Inhibitor Cocktail (Thermo Scientific)) for at least 15 minutes. Then the pronuclei were washed once through PBS and 1x NEB3 buffer (NEB) with 0.6% SDS, in which they were then incubated at 37° for 2 hours with shaking in humidified atmosphere. Then pronuclei were washed once in 1x DpnII buffer (NEB) with 2x BSA (NEB), and then chromatin was digested overnight in 9ul of the same solution but with 5 U DpnII (NEB). The nuclei were then washed once through PBS, then through 1xT4 ligase buffer (50 mM Tris-HCl, 10 mM $MgCl_2$, 1 mM ATP, 10 mM DTT, pH 7.5). Then the nuclei were incubated in the same buffer but with 5U T4 DNA ligase (Thermo Scientific) at 16° with 50 rpm rotation for 4.5 hours, and then for 30 min at room temperature. Whole-genome amplification was performed using illustra GenomiPhi v2 DNA amplification kit (GE Healthcare) with decrosslinking nuclei at 65° overnight in sample buffer. High molecular weight DNA was purified using AMPure XP beads (Beckman Coulter), and 1 ug was used to prepare Illumina libraries for sequencing (by VBCF NGS Unit, csf.ac.at) after sonicating to ~300-1300 bp. Libraries were sequenced on HiSeq 2500 v4 with 125 bp paired end reads (at VBCF) or on

NextSeq high output lane with 75 bp paired end reads (at Wellcome Trust Clinical Research Facility, Edinburgh), between 10 and 24 cells per lane.

DNA and Scc1 staining

After zygote collection, the cells were fixed in 4% PFA for 30 min, before permeabilization in 0.2% Triton X-100/PBS (PBSTX) for 30 min. Cells were then blocked in 10% goat serum (Dako) in PBSTX either at 4C overnight or for several hours at 4C followed by room temperature incubation. Cells were incubated overnight at 4C in primary antibody (anti-Scc1, Millipore #05-908, 1:250). After washing in blocking solution for at least 30 min, incubation with the secondary antibody (anti-mouse IgG (H+L), Thermo Fisher Scientific #A-11001, 1:500) was carried out for 1h at room temperature. Another set of washing steps in 0.2% Triton X-100/PBS was followed by a quick PBS wash and mounting of the cells in Vectashield containing DAPI (Vector labs) using imaging spacers (Sigma Aldrich). *In situ* fixed zygotes were imaged on a confocal microscope (LSM780, Zeiss, ZEN black) using a 63x, 1.4NA oil objective. Presence of DNA compaction reminiscent of vermicelli in Wapl zygotes was classified using ImageJ and 3D visualization by Imaris (8.1.2). Brightness and contrast of images presented were adjusted using ImageJ software. No blinding or randomization were used for handling of the cells. Samples were excluded from the analysis if cells were not fertilized or in the wrong cell cylcle phase (PN stage).

Antibodies

Anti-Rad21 (anti-Scc1, 1:250, Millipore, Cat# 05-908; RRID: AB_417383); Goat anti-Mouse IgG (H+L) Cross-Adsorbed Secondary Antibody (1:500, Alexa Fluor 488, Thermo Fisher Scientific, Cat# A-11001; RRID: AB_2534069).

Live-cell imaging of Scc1-EGFP

In vitro fertilization after *in vitro* maturation was performed as described before (Ladstätter and Tachibana-Konwalski, 2017). Oocytes from 2-5 month old females were isolated by puncturing of ovaries with hypodermic needles in the presence of 0.2 mM IBMX, 20% FBS (Gibco) and 6 mg/ml fetuin (Sigma Aldrich). After microinjection of oocytes with H2B-mCherry (187 ng/µl) and Scc1-EGFP (260 ng/µl), oocytes were cultured for 1-1.5 h and then released from IBMX inhibition by washing in M16. Following *in vitro* maturation in the incubator (low oxygen conditions: 5% CO_2, 5% O_2, 90% N_2; 37°C), cells were scored for extrusion of the first polar body and MII eggs were *in vitro* fertilized 10.5-12 hours post release from IBMX inhibition. The sperm was obtained from the *cauda epididimis* and *vas deferens* of B6CBAF1 stud males and was capacitated in fertilization medium (Cook) in a tilted cell culture dish for at least 30 min. Motile sperm from the surface of the dish was used for *in vitro* fertilization of the *in vitro* maturated eggs. After 3-3.5 h zygotes were washed in M16 and imaged. Live-cell imaging of zygotes microinjected with fluorescent fusion proteins was performed on a confocal microscope (LSM 800, Zeiss; ZEN blue) equipped with an incubation chamber suited for live-cell imaging (5% CO_2, 37°C). Zygotes were kept in ~3µl cleavage medium (Research Vitro Cleave, Cooks Austria GmbH) under mineral oil (Sigma Aldrich or Millipore) for the duration of the imaging. Movies were taken using a 63x, 1.20NA water immersion objective, taking 25 z-slices (48µm) every 10 minutes. Brightness and contrast of images presented were adjusted using ImageJ software. No blinding or randomization were used for handling of the cells. Samples were excluded from the analysis if cells were not fertilized.

snHi-C data analysis

snHi-C data were processed similarly as in (Flyamer et al., 2017) and detailed information of single cell and pooled data is given in **Table EV1** and **EV2**. Briefly, reads were mapped to the mm9 genome using *hiclib* (which applies iterative mapping with *bowtie2*) and then filtered. These data were then converted into *Cooler* files with heatmaps at different resolutions for downstream analysis.

We applied the same methods for quantification of different features of spatial organization of the genome as previously (Flyamer et al., 2017). Briefly, we used GC-content as a proxy for A/B compartmentalization signal and constructed 5x5 percentile-binned matrices to quantify strength of compartment segregation (also called "saddle plots" for compartments). These 5x5 matrices were then iteratively corrected (Imakaev et al., 2012). For average analysis of TADs we used published TAD coordinates (Rao et al., 2014) for the CH12-LX mouse cell line. We averaged Hi-C maps of all TADs and their neighbouring regions, chosen to be of the same length as the TAD, after rescaling each TAD to a 90x90 matrix. For visualization, the contact probability of these matrices was rescaled to follow a shallow power law with distance (-0.25 scaling) (see **Appendix Figure S1A**). Similarly, we analyzed loops by summing up snHi-C contact frequencies for loop coordinates identified in Rao et al., 2014 for CH12-LX mouse cells. By averaging 20x20 matrices surrounding the loops and dividing the final result by similarly averaged control matrices, we removed the effects of distance-dependence (see **Appendix Figure S1A**). Control loop matrices were obtained by averaging 20x20 matrices centered on the locations of randomly shifted positions of known loops; shifts ranged from 100 to 1100 Kb with 100 shifts for each loop. For display and visual consistency with the loop strength quantification, we set the background levels of interaction to 1; the background is defined as the green boxes in **Figure EV 3A** described below.

For the quantification of loop strength, we divided the average signal in the middle 6x6 submatrix by the average signal in top-left and bottom-right (at the same distance from the main diagonal) 6x6 submatrices (see **Figure EV 3A**). To obtain the 95% confidence intervals on the loop strengths we applied bootstrapping: using the pooled single cell data, we randomly sampled N loops with replacement (where N equals the total number of loops used in the original samples), and calculated the loop strengths from this random sample. We performed this procedure 10,000 times for each condition, using the sorted set of 10,000 strength values to obtain the confidence intervals.

TAD strength was quantified using $P_c(s)$ normalized snHi-C data (see **Appendix Figure S1A** bottom left panel). In python notation, if M is the 90x90 TAD numpy array (where numpy is np), L = 90 is the length of the matrix, then TAD_strength = box1/box2, where:

```
box1= 0.5*np.sum(M[0:L//3,L//3:2*L//3])+0.5*np.sum( M[L//3:2*L//3, 2*L//3:L])

box2 = np.sum(M[L//3:2*L//3,L//3:2*L//3])
```

Compartment saddle plot strength was quantified by the formula: log(AA*BB/(AB*BA)), where AA, AB, BA, BB represent the 4 corners of the iteratively corrected saddle plot matrix.

To calculate the insulation score, we computed the sum of read counts within a sliding 40 kb by 40 kb diamond. The diamond was positioned such that the "tip" touched the main axis of the snHi-C map corresponding to a "self-interaction". Since snHi-C maps are not iteratively corrected, we normalized all insulation profiles by the score of the minimum insulation, and then subtracted 1. This way, the insulation/domain boundary is at 0, and has a minimum of 0.

Contact probability, $P_c(s)$, curves were computed from 10 kb binned snHi-C data. We divided the linear genomic separations into logarithmic bins with a factor of 1.3. Data within these log-spaced bins (at distance, s) were averaged to produce the value of $P_c(s)$. In **Figure 3,** both $P_c(s)$ curves and their log-space slopes are shown following a gaussian smoothing (using the scipy.ndimage.filters.gaussian_smoothing1d function with radius 0.8). Both the y-axis (i.e. $\log(P_c(s))$ and the x-axis (i.e. log(s)) were smoothed.

De novo TAD boundary calling

TAD boundaries were called de novo on multiple cell types using the corner score as described in Schwarzer et al., 2017 using default parameters. Hi-C data for this analysis were processed using *hiclib* as described (Imakaev et al., 2012) and files were converted to *Cool* format.

Sorting maternal and paternal cells

As described previously (Flyamer et al., 2017), it is possible to distinguish maternally and paternally derived chromatin based on the shape of the $P_c(s)$ curve in single cells. Maternal chromatin has a characteristic plateau/flattening of the $P_c(s)$ at 10 Mb-30 Mb. Due to the similar pronucleus sizes of the Scc1 control data which made them difficult to sort post-lysis, we opted to sort maternal and paternal pronuclei in-silico. We chose a separate cutoff-value for $P_c(s)$ for G1-phase (Scc1 controls and knockout) and G2-phase cells (G2, Wapl controls and knockout) that was used to designate maternal or paternal chromatin as the $P_c(s)$ curve changes through the cell cycle. First, we normalized all $P_c(s)$ curves to 1 at 9 kb for all conditions. For G1 cells, all $P_c(s)$ curves with a value above $1x10^{-4}$ at 15 Mb were designated maternal. For G2 cells, all $P_c(s)$ curves with a value above $2.5x10^{-5}$ at 20 Mb were designated maternal. Cells in which the pronuclei were stuck together after lysis were given the tag "both", and were not assigned a maternal/paternal value in-silico, but were used in the "combined" data analyses of Figure 2. We further filtered out bad data using the cutoff of $P_c(s) < 10^{-1}$ at 30 kb; these cells were excluded from all analyses.

Analysis of Du et al., 2017 data

Pre-processed, mapped valid pair files were obtained from GEO accession number GSE82185. These files were directly converted to the *Cooler* format (https://github.com/mirnylab/cooler) without any further filtering or processing using csort and cload functions. Averaging analysis for loops, TADs, compartments were performed as described previously (Flyamer et al., 2017) and summarized in the above section.

Analyses of Ke et al., 2017 data

FASTQ files were downloaded from BioProject, identifier PRJCA000241 (http://bigd.big.ac.cn/bioproject/browse/PRJCA000241) . Data were mapped to the mm9 genome and converted to *Cooler* format using distiller (https://github.com/mirnylab/distiller-nf). Averaging analyses for loops, TADs and compartments were performed as described previously (Flyamer et al., 2017).

Polymer simulations

Polymer simulations of loop extrusion were performed as in (Flyamer et al., 2017), but using updates to the simulation engine (Fudenberg et al., 2017). The simulation engine is build using the openmm-polymer package which relies on OpenMM-7 (Eastman et al., 2017). Parameters for simulations were as follows: 2000 MD steps per loop extrusion step. Simulations were performed either using N=30,000 monomers, or N=100,000 monomers. Simulations were initialized using a fractal globule or a mitotic chromosome model, as described in (Flyamer et al., 2017). Bi-directional TAD boundaries were placed at monomers 0, 1200, 1500, 2000,2900, 3900, 4300, 4800, 5600, 6100, 6500, 7600, 8300, 8900, 9500; and at positions shifted by multiples of 10,000 (10000, 11200, 11500, 12000, … 20000, 21200, 21500, 22000…). TAD boundaries were implemented as monomers that pause the loop extruding factor (LEF) translocation with probability 99.5 %. That would delay translocation of a LEF by on average 200 loop extrusion steps. All simulations were performed in periodic boundary conditions at a given density. For each simulation, we simulated 4000 steps of loop extrusion dynamics, starting with a random placement of LEFs at the beginning of a simulation.

We performed two types of simulations. A parameter sweep for processivity-separation values was performed for a system of 30,000 monomers for all pairwise combinations of the values of

processivity of 60, 120, 240, 480, and 960kb, and the values of separation of 30, 60, 120, 240, 480, and 2400kb. The largest value of separation was to simulate 20-fold depletion of LEFs relative to WT model value of 120kb (Fudenberg et al., 2016). All simulations here were initialized with a 30,000 fragment of a mitotic chromosome model. We used density of 0.02 for these simulations.

A more complete simulation was performed using a system of 100,000 monomers, initialized from a mitotic chromosome model, or from a fractal globule for maternal and paternal chromosomes, respectively. Particular values of parameters were chosen based on a parameter sweep. We chose values of processivity and separation of 120kb for the control conditions model, the same values as used in (Fudenberg et al., 2016). For the model of SCC1 knock-out, we reduced the number of cohesins 20-fold, which corresponds to increasing separation to 2400kb. For the model of WAPL knock-out of maternal chromatin, we increased processivity 4-fold, but kept the separation at 120 kb. For WAPL knock-out of paternal chromatin, we best matched the difference in $P_c(s)$ in the s=100-500kb region by decreasing the processivity two-fold, but increasing separation by two-fold as compared to maternal. Additionally, to reflect the larger paternal pronuclear volume, we decreased the density of simulations two-fold, to 0.01.

We calculated $P_c(s)$ and simulated contact maps using a contact radius of 5 monomers. Both $P_c(s)$ curves and their log-space slopes are shown following a gaussian smoothing (using the scipy.ndimage.filters.gaussian_smoothing1d function with radius 0.8). Both the y-axis (i.e. $\log(P_c(s))$ and the x-axis (i.e. log(s)) were smoothed.

Data and software availability

The snHi-C data has been deposited on NCBI GEO under the accession number: GSE100569. Polymer simulation code is available in the "examples" directory of the openmm-polymer library (https://bitbucket.org/mirnylab/openmm-polymer); analysis code of polymer configurations, including the surface area and volume measurements will be made available upon publication. snHi-C data processing code has been released as an example for the hiclib package (https://bitbucket.org/mirnylab/hiclib).

AUTHOR CONTRIBUTIONS

J.G. and H.B.B. contributed equally. K.T.-K. conceived the project. J.G. supervised by K.T.-K. performed snHi-C and imaging experiments. H.B.B. supervised by L.A.M. developed and performed snHi-C data analysis and simulations. M.I. performed simulations. I.M.F. performed image analysis. S.L. provided novel mouse strains and imaging reagents. J.M.P. provided a novel mouse strain. H.B.B., J.G., M.I. and I.M.F. prepared the figures. H.B.B., J.G., M.I., I.M.F., W.A.B., L.A.M. and K.T.-K. wrote the manuscript with input from all authors.

CONFLICT OF INTEREST

The authors declare that they have no conflict of interest.

ACKNOWLEDGEMENTS

We thank M. Coelho Correia da Silva and M. H. Idarraga-Amado for providing conditional *Wapl* mice and reagents, and A. Hirsch, K. Klien and N. Laumann-Lipp for technical assistance with pronuclear extractions. We are grateful to J. Nuebler for discussions and suggestions for simulations and sharing codes, and to A. Goloborodko for suggesting the derivative-based analyses of $P_c(s)$ curves. Illumina sequencing was performed at the VBCF NGS Unit (http://www.vbcf.ac.at) and Edinburgh Wellcome Trust Clinical Research Facility (WTCRF). We thank the staff of Vienna Biocenter BioOptics facility for assistance with imaging and analysis. J.G. is an associated student of the DK Chromosome Dynamics (W1238-B20) supported by the Austrian Science Fund (FWF) and the European Research Council. H.B.B. is grateful for support by the Natural Sciences and Engineering Research Council of Canada, PGS-D. I.M.F. is grateful for support from the Darwin Trust of Edinburgh. W.A.B. is supported by the UK Medical Research Council. This work was funded by the Austrian Academy of Sciences and by the ERC-StG-336460 ChromHeritance grant to K.T.-K.. The work in the Mirny laboratory is supported by R01 GM114190, U54 DK107980 from the National Institute of Health, and 1504942 from the National Science Foundation.

REFERENCES

Adenot PG, Mercier Y, Renard JP & Thompson EM (1997) Differential H4 acetylation of paternal and maternal chromatin precedes DNA replication and differential transcriptional activity in pronuclei of 1-cell mouse embryos. *Development* **124:** 4615–4625

Aoki F, Worrad DM & Schultz RM (1997) Regulation of transcriptional activity during the first and second cell cycles in the preimplantation mouse embryo. *Dev. Biol.* **181:** 296–307

Burkhardt S, Borsos M, Szydlowska A, Godwin J, Williams SA, Cohen PE, Hirota T, Saitou M & Tachibana-Konwalski K (2016) Chromosome Cohesion Established by Rec8-Cohesin in Fetal Oocytes Is Maintained without Detectable Turnover in Oocytes Arrested for Months in Mice. *Curr. Biol.* **26:** 678–685

Ciosk R, Shirayama M, Shevchenko A, Tanaka T, Toth A, Shevchenko A & Nasmyth K (2000) Cohesin's Binding to Chromosomes Depends on a Separate Complex Consisting of Scc2 and Scc4 Proteins. *Mol. Cell* **5:** 243–254

Deardorff MA, Kaur M, Yaeger D, Rampuria A, Korolev S, Pie J, Gil-Rodríguez C, Arnedo M, Loeys B, Kline AD, Wilson M, Lillquist K, Siu V, Ramos FJ, Musio A, Jackson LS, Dorsett D & Krantz ID (2007) Mutations in Cohesin Complex Members SMC3 and SMC1A Cause a Mild Variant of Cornelia de Lange Syndrome with Predominant Mental Retardation. *Am. J. Hum. Genet.* **80:** 485–494

Dixon JR, Selvaraj S, Yue F, Kim A, Li Y, Shen Y, Hu M, Liu JS & Ren B (2012) Topological domains in mammalian genomes identified by analysis of chromatin interactions. *Nature* **485:** 376–380

Du Z, Zheng H, Huang B, Ma R, Wu J, Zhang X, He J, Xiang Y, Wang Q, Li Y, Ma J, Zhang X, Zhang K, Wang Y, Zhang MQ, Gao J, Dixon JR, Wang X, Zeng J & Xie W (2017) Allelic reprogramming of 3D chromatin architecture during early mammalian development. *Nature* **547:** 232–235

Eastman P, Swails J, Chodera JD, McGibbon RT, Zhao Y, Beauchamp KA, Wang L-P, Simmonett AC, Harrigan MP, Stern CD, Wiewiora RP, Brooks BR & Pande VS (2017) OpenMM 7: Rapid development of high performance algorithms for molecular dynamics. *PLOS Comput. Biol.* **13:** e1005659

Flavahan WA, Drier Y, Liau BB, Gillespie SM, Venteicher AS, Stemmer-Rachamimov AO, Suvà ML & Bernstein BE (2015) Insulator dysfunction and oncogene activation in IDH mutant gliomas. *Nature* **529:** 110–114

Flyamer IM, Gassler J, Imakaev M, Brandão HB, Ulianov S V., Abdennur N, Razin S V., Mirny LA & Tachibana-Konwalski K (2017) Single-nucleus Hi-C reveals unique chromatin reorganization at oocyte-to-zygote transition. *Nature* **544:** 110–114

Franke M, Ibrahim DM, Andrey G, Schwarzer W, Heinrich V, Schöpflin R, Kraft K, Kempfer R, Jerković I, Chan W-L, Spielmann M, Timmermann B, Wittler L, Kurth I, Cambiaso P, Zuffardi O, Houge G, Lambie L, Brancati F, Pombo A, et al (2016) Formation of new chromatin domains determines pathogenicity of genomic duplications. *Nature* **538:** 265–269

Fudenberg G & Imakaev M (2017) FISH-ing for captured contacts: towards reconciling FISH and 3C. *Nat. Methods* **14:** 673–678

Fudenberg G, Imakaev M, Lu C, Goloborodko A, Abdennur N & Mirny LA (2016) Formation of Chromosomal Domains by Loop Extrusion. *Cell Rep.* **15:** 2038–2049

Gandhi R, Gillespie PJ & Hirano T (2006) Human Wapl Is a Cohesin-Binding Protein that Promotes Sister-Chromatid Resolution in Mitotic Prophase. *Curr. Biol.* **16:** 2406–2417

Giorgetti L, Lajoie BR, Carter AC, Attia M, Zhan Y, Xu J, Chen CJ, Kaplan N, Chang HY, Heard E & Dekker J (2016) Structural organization of the inactive X chromosome in the mouse. *Nature* **535:** 575–579

Goloborodko A, Marko JF & Mirny LA (2016) Chromosome Compaction by Active Loop Extrusion. *Biophys. J.* **110:** 2162–2168

Haarhuis JHI, van der Weide RH, Blomen VA, Yáñez-Cuna JO, Amendola M, van Ruiten MS, Krijger PHL, Teunissen H, Medema RH, van Steensel B, Brummelkamp TR, de Wit E & Rowland BD (2017) The Cohesin Release Factor WAPL Restricts Chromatin Loop Extension. *Cell* **169:** 693–707.e14

Halverson JD, Smrek J, Kremer K & Grosberg AY (2014) From a melt of rings to chromosome territories: the role of topological constraints in genome folding. *Rep. Prog. Phys.* **77:** 22601

Hamatani T, Carter MG, Sharov AA & Ko MSH (2004) Dynamics of Global Gene Expression Changes during Mouse Preimplantation Development. *Dev. Cell* **6:** 117–131

Hansen AS, Pustova I, Cattoglio C, Tjian R & Darzacq X (2017) CTCF and cohesin regulate chromatin loop stability with distinct dynamics. *Elife* **6:**

van der Heijden GW, Dieker JW, Derijck AAHA, Muller S, Berden JHM, Braat DDM, van der Vlag J & de Boer P (2005) Asymmetry in Histone H3 variants and lysine methylation between paternal and maternal chromatin of the early mouse zygote. *Mech. Dev.* **122:** 1008–1022

Hug CB, Grimaldi AG, Kruse K & Vaquerizas JM (2017) Chromatin Architecture Emerges during Zygotic Genome Activation Independent of Transcription. *Cell* **169:** 216–228.e19

Imakaev M, Fudenberg G, McCord RP, Naumova N, Goloborodko A, Lajoie BR, Dekker J & Mirny LA (2012) Iterative correction of Hi-C data reveals hallmarks of chromosome organization. *Nat. Methods* **9:** 999–1003

Inoue A, Jiang L, Lu F, Suzuki T & Zhang Y (2017) Maternal H3K27me3 controls DNA methylation-independent imprinting. *Nature* **547:** 419–424

Ke Y, Xu Y, Chen X, Feng S, Liu Z, Sun Y, Yao X, Li F, Zhu W, Gao L, Chen H, Du Z, Xie W, Xu X, Huang X & Liu J (2017) 3D Chromatin Structures of Mature Gametes and Structural Reprogramming during Mammalian Embryogenesis. *Cell* **170:** 367–381.e20

Krantz ID, McCallum J, DeScipio C, Kaur M, Gillis LA, Yaeger D, Jukofsky L, Wasserman N, Bottani A, Morris CA, Nowaczyk MJM, Toriello H, Bamshad MJ, Carey JC, Rappaport E, Kawauchi S, Lander AD, Calof AL, Li H, Devoto M, et al (2004) Cornelia de Lange syndrome is caused by mutations in NIPBL, the human homolog of Drosophila melanogaster Nipped-B. *Nat. Genet.* **36:** 631–635

Kueng S, Hegemann B, Peters BH, Lipp JJ, Schleiffer A, Mechtler K & Peters J-M (2006) Wapl Controls the Dynamic Association of Cohesin with Chromatin. *Cell* **127:** 955–967

Ladstätter S & Tachibana-Konwalski K (2016) A Surveillance Mechanism Ensures Repair of DNA Lesions during Zygotic Reprogramming. *Cell* **167:** 1774–1787.e13

Lan Z-J, Xu X & Cooney AJ (2004) Differential Oocyte-Specific Expression of Cre Recombinase Activity in GDF-9-iCre, Zp3cre, and Msx2Cre Transgenic Mice1. *Biol. Reprod.* **71:** 1469–1474

Lewandoski M, Wassarman KM & Martin GR (1997) Zp3–cre, a transgenic mouse line for the activation or inactivation of loxP-flanked target genes specifically in the female germ line. *Curr. Biol.* **7:** 148–151

Lopez-Serra L, Lengronne A, Borges V, Kelly G & Uhlmann F (2013) Budding yeast Wapl controls sister chromatid cohesion maintenance and chromosome condensation. *Curr. Biol.* **23:** 64–9

Lupiáñez DG, Kraft K, Heinrich V, Krawitz P, Brancati F, Klopocki E, Horn D, Kayserili H, Opitz JM, Laxova R, Santos-Simarro F, Gilbert-Dussardier B, Wittler L, Borschiwer M, Haas SA, Osterwalder M, Franke M, Timmermann B, Hecht J, Spielmann M, et al (2015) Disruptions of Topological Chromatin Domains Cause Pathogenic Rewiring of Gene-Enhancer Interactions. *Cell* **161:** 1012–1025

Mayer W, Niveleau A, Walter J, Fundele R & Haaf T (2000) Demethylation of the zygotic paternal genome. *Nature* **403:** 501–502

Mizuguchi T, Fudenberg G, Mehta S, Belton J-M, Taneja N, Folco HD, FitzGerald P, Dekker J, Mirny L, Barrowman J & Grewal SIS (2014) Cohesin-dependent globules and heterochromatin shape 3D genome architecture in S. pombe. *Nature* **516:** 432–435

Musio A, Selicorni A, Focarelli ML, Gervasini C, Milani D, Russo S, Vezzoni P & Larizza L (2006) X-linked Cornelia de Lange syndrome owing to SMC1L1 mutations. *Nat. Genet.* **38:** 528–530

Nagano T, Lubling Y, Várnai C, Dudley C, Leung W, Baran Y, Mendelson Cohen N, Wingett S, Fraser P & Tanay A (2017) Cell-cycle dynamics of chromosomal organization at single-cell resolution. *Nature* **547:** 61–67

Naumova N, Imakaev M, Fudenberg G, Zhan Y, Lajoie BR, Mirny L a & Dekker J (2013a) Organization of the mitotic chromosome. *Science* **342:** 948–53

Naumova N, Imakaev M, Fudenberg G, Zhan Y, Lajoie BR, Mirny LA & Dekker J (2013b) Organization of the Mitotic Chromosome. *Science (80-.).* **342:** 948–953

Nolen LD, Boyle S, Ansari M, Pritchard E & Bickmore WA (2013) Regional chromatin decompaction in Cornelia de Lange syndrome associated with NIPBL disruption can be uncoupled from cohesin and CTCF. *Hum. Mol. Genet.* **22:** 4180–93

Nora EP, Goloborodko A, Valton A-L, Gibcus JH, Uebersohn A, Abdennur N, Dekker J, Mirny LA & Bruneau BG (2017) Targeted Degradation of CTCF Decouples Local Insulation of Chromosome Domains from Genomic Compartmentalization. *Cell* **169:** 930–944.e22

Nora EP, Lajoie BR, Schulz EG, Giorgetti L, Okamoto I, Servant N, Piolot T, van Berkum NL, Meisig J, Sedat J, Gribnau J, Barillot E, Blüthgen N, Dekker J & Heard E (2012) Spatial partitioning of the regulatory landscape of the X-inactivation centre. *Nature* **485:** 381–5

Nuebler J, Fudenberg G, Imakaev M, Abdennur N & Mirny L (2017) Chromatin Organization by an Interplay of Loop Extrusion and Compartmental Segregation. *bioRxiv* doi: https://doi.org/10.1101/196261

Oswald J, Engemann S, Lane N & Mayer W (2000) Active demethylation of the paternal genome in the mouse zygote. *Curr. Biol.*: 475–478

Parelho V, Hadjur S, Spivakov M, Leleu M, Sauer S, Gregson HC, Jarmuz A, Canzonetta C, Webster Z, Nesterova T, Cobb BS, Yokomori K, Dillon N, Aragon L, Fisher AG & Merkenschlager M (2008) Cohesins Functionally Associate with CTCF on Mammalian Chromosome Arms. *Cell* **132:** 422–433

Peters J-M, Tedeschi A & Schmitz J (2008) The cohesin complex and its roles in chromosome biology. *Genes Dev.* **22:** 3089–3114

Phillips-Cremins JE, Sauria MEG, Sanyal A, Gerasimova TI, Lajoie BR, Bell JSK, Ong C-T, Hookway TA, Guo C, Sun Y, Bland MJ, Wagstaff W, Dalton S, McDevitt TC, Sen R, Dekker J, Taylor J & Corces VG (2013) Architectural Protein Subclasses Shape 3D Organization of Genomes during Lineage Commitment. *Cell* **153:** 1281–1295

Rao SSP, Huang S-C, Glenn St Hilaire B, Engreitz JM, Perez EM, Kieffer-Kwon K-R, Sanborn AL, Johnstone SE, Bascom GD, Bochkov ID, Huang X, Shamim MS, Shin J, Turner D, Ye Z, Omer AD, Robinson JT, Schlick T, Bernstein BE, Casellas R, et al (2017) Cohesin Loss Eliminates All Loop Domains. *Cell* **171:** 305–320.e24

Rao SSP, Huntley MH, Durand NC, Stamenova EK, Bochkov ID, Robinson JT, Sanborn AL, Machol I, Omer AD, Lander ES & Aiden EL (2014) A 3D map of the human genome at kilobase resolution reveals principles of chromatin looping. *Cell* **159:** 1665–1680

Rodman TC, Pruslin FH, Hoffmann HP & Allfrey VG (1981) Turnover of basic chromosomal proteins in fertilized eggs: a cytoimmunochemical study of events in vivo. *J. Cell Biol.* **90:** 351–61

Sanborn AL, Rao SSP, Huang S-C, Durand NC, Huntley MH, Jewett AI, Bochkov ID, Chinnappan D, Cutkosky A, Li J, Geeting KP, Gnirke A, Melnikov A, McKenna D, Stamenova EK, Lander ES & Aiden EL (2015) Chromatin extrusion explains key features of loop and domain formation in wild-type and engineered genomes. *Proc. Natl. Acad. Sci.* **112:** 201518552

Santos F, Peat J, Burgess H, Rada C, Reik W & Dean W (2013) Active demethylation in mouse zygotes involves cytosine deamination and base excision repair. *Epigenetics Chromatin* **6:** 39

Schwarzer W, Abdennur N, Goloborodko A, Pekowska A, Fudenberg G, Loe-Mie Y, Fonseca NA, Huber W, Haering C, Mirny L & Spitz F (2017) Two independent modes of chromatin organization revealed by cohesin removal. *Nature*

Seitan VC, Faure AJ, Zhan Y, McCord RP, Lajoie BR, Ing-Simmons E, Lenhard B, Giorgetti L, Heard E, Fisher AG, Flicek P, Dekker J & Merkenschlager M (2013) Cohesin-based chromatin interactions enable regulated gene expression within preexisting architectural compartments. *Genome Res.* **23:** 2066–2077

Sofueva S, Yaffe E, Chan W-C, Georgopoulou D, Vietri Rudan M, Mira-Bontenbal H, Pollard SM, Schroth GP, Tanay A & Hadjur S (2013) Cohesin-mediated interactions organize chromosomal domain architecture. *EMBO J.* **32:** 3119–3129

Tachibana-Konwalski K, Godwin J, van der Weyden L, Champion L, Kudo NR, Adams DJ & Nasmyth K (2010) Rec8-containing cohesin maintains bivalents without turnover during the growing phase of mouse oocytes. *Genes Dev.* **24:** 2505–16

Tedeschi A, Wutz G, Huet S, Jaritz M, Wuensche A, Schirghuber E, Davidson IF, Tang W, Cisneros DA, Bhaskara V, Nishiyama T, Vaziri A, Wutz A, Ellenberg J & Peters J-M (2013) Wapl is an essential regulator of chromatin structure and chromosome segregation. *Nature* **501:** 564–568

Terakawa T, Bisht S, Eeftens JM, Dekker C, Haering CH & Greene EC (2017) The condensin complex is a mechanochemical motor that translocates along DNA. *Science (80-.).***:** eaan6516

Tjong H, Gong K, Chen L & Alber F (2012) Physical tethering and volume exclusion determine higher-order genome organization in budding yeast. *Genome Res.* **22:** 1295–305

Tonkin ET, Wang T-J, Lisgo S, Bamshad MJ & Strachan T (2004) NIPBL, encoding a homolog of fungal Scc2-type sister chromatid cohesion proteins and fly Nipped-B, is mutated in Cornelia de Lange syndrome. *Nat. Genet.* **36:** 636–641

Torres-Padilla M-E, Bannister AJ, Hurd PJ, Kouzarides T & Zernicka-Goetz M (2006) Dynamic distribution of the replacement histone variant H3.3 in the mouse oocyte and preimplantation embryos. *Int. J. Dev. Biol.* **50:** 455–61

Tran NT, Laub MT & Le TBK (2017) SMC Progressively Aligns Chromosomal Arms in Caulobacter crescentus but Is Antagonized by Convergent Transcription. *Cell Rep.* **20:** 2057–2071

Ulianov S V., Tachibana-Konwalski K & Razin S V. (2017) Single-cell Hi-C bridges microscopy and genome-wide sequencing approaches to study 3D chromatin organization. *BioEssays***:** 1700104

Vietri Rudan M, Barrington C, Henderson S, Ernst C, Odom DT, Tanay A & Hadjur S (2015) Comparative Hi-C Reveals that CTCF Underlies Evolution of Chromosomal Domain Architecture. *Cell Rep.* **10:** 1297–1309

Wang X, Brandão HB, Le TBK, Laub MT & Rudner DZ (2017) Bacillus subtilis SMC complexes juxtapose chromosome arms as they travel from origin to terminus. *Science (80-.).* **355:** 524–527

Wendt KS, Yoshida K, Itoh T, Bando M, Koch B, Schirghuber E, Tsutsumi S, Nagae G, Ishihara K, Mishiro T, Yahata K, Imamoto F, Aburatani H, Nakao M, Imamoto N, Maeshima K, Shirahige K & Peters J-M (2008) Cohesin mediates transcriptional insulation by CCCTC-binding factor. *Nature* **451:** 796–801

Wutz G, Varnai C, Nagasaka K, Cisneros DA, Stocsits R, Tang W, Schoenfelder S, Jessberger G, Muhar M, Hossain JM, Walther N, Koch B, Kueblbeck M, Ellenberg J, Zuber J, Fraser P & Peters J-M (2017) CTCF, WAPL and PDS5 proteins control the formation of TADs and loops by cohesin. *bioRxiv* doi: https://doi.org/10.1101/177444

Zhang Y, Vastenhouw NL, Feng J, Fu K, Wang C, Ge Y, Pauli A, van Hummelen P, Schier AF, Liu XS, Schier A, Kelsh R, Odenthal J, Warga R, Nüsslein-Volhard C, Rathert P, Jude J, Ferrari F, Blanco A, Fellner M, et al (2014) Canonical nucleosome organization at promoters forms during genome activation. *Genome Res.* **24:** 260–6

Zuin J, Dixon JR, van der Reijden MIJA, Ye Z, Kolovos P, Brouwer RWW, van de Corput MPC, van de Werken HJG, Knoch TA, van IJcken WFJ, Grosveld FG, Ren B & Wendt KS (2014) Cohesin and

CTCF differentially affect chromatin architecture and gene expression in human cells. *Proc. Natl. Acad. Sci.* **111:** 996–1001

MAIN FIGURE LEGENDS

Figure 1: Relationship between single-cell and population Hi-C maps in light of the loop extrusion model

A. A schematic illustration for the loop extrusion mechanism.The model posits that cohesin processively extrudes chromatin loops, and is hindered by other cohesins or boundary elements like CTCF.

B. We illustrate the distinction between cohesin-extruded loops which result in variable contacts in single-cell maps, and Hi-C loops which represent a population-average picture of extruded loops stalled at boundary elements. TADs in population Hi-C maps are generated by cohesin-extruded loops.

Figure 2: Zygotic chromatin is organized into loops, TADs and compartments that change during the first cell cycle

A. Embryonic development from fertilization of the metaphase II egg by sperm, to zygote formation and division, to the 2-cell embryo. Maternal and paternal genomes form separate nuclei in the zygote. The major zygotic genome activation (ZGA) occurs in the 2-cell mouse embryo.

B. Average chromatin loops, TADs and compartments are detectable in maternal and paternal chromatin from the one-cell embryo onwards; data re-analyzed from Du et al., 2017. Zygotic pronuclear stage 3 (PN3) and stage 5 correspond to S and G2 phases, respectively. The average strength of each feature is shown inset into each corresponding panel (see **Materials and Methods**).

C. We *de novo* annotated TAD boundaries (see **Methods and Materials**) in mouse ES cells (Nora et al., 2017) and show that TADs in wild-type zygotes are detected (Flyamer et al., 2017). To further verify that TAD detection in zygotes is insensitive to the choice of annotated boundaries see **Figure EV 1**.

D. The strength of average loops, TADs and compartments becomes more similar between the maternal and paternal genomes as the zygotic cell cycle progresses (G1/S: Flyamer et al., 2017, G2: this work, n(maternal)= 18 and n(paternal)= 13 nuclei, based on two independent experiments using five and six females).

E. Loop strengths in G1/S and G2 phase maternal and paternal chromatin of zygotes are the reported as the fractional enrichment above background levels (see **Methods and Materials**). Error bars displayed are the 95% confidence intervals obtained by bootstrapping.

Figure 3: Conditional genetic knockouts of *Scc1* and *Wapl* reveal cohesin's essential role in formation of loops and TADs in mouse zygotes

A. Generation of conditional genetic knockout oocytes by *Zp3*-Cre recombinase in post-recombination growing phase mouse oocytes. Fertilization produces maternal knockout zygotes (maternal, m, paternal, p, alleles). Maternal and paternal nuclei are extracted from zygotes before being subjected separately to snHi-C.

B. Average loops, TADs and compartments in control ($Wapl^{fl}$ and $Scc1^{fl}$), $Scc1^{\Delta}$ and $Wapl^{\Delta}$ zygotes. Both maternal and paternal data are shown pooled together. Data is based on n($Wapl^{fl}$)= 17, n($Wapl^{\Delta}$)= 17, n($Scc1^{fl}$)=30, n($Scc1^{\Delta}$)=45 nuclei, from at least two independent experiments using two to three females per genotype each.

C. Separation of loops by size for control, $Scc1^{\Delta}$ and $Wapl^{\Delta}$ zygotes for maternal and paternal data pooled together.

D. Loop strengths are reported as the fractional enrichment above background levels (see **Materials and Methods**). Error bars displayed are the 95% confidence intervals obtained by bootstrapping pooled single cell loops.

Figure 4. Differences in genome-wide contact probability, $P_c(s)$, for chromatin loci separated by genomic distances, s, between conditions.

A-C. Experimental $P_c(s)$ for maternal and paternal chromatin for *Scc1* control, $Scc1^{\Delta}$ and $Wapl^{\Delta}$ conditions. Black solid lines in B and C show the control curves as a reference to guide the eye. Slopes of the log($P_c(s)$) curves for each condition are shown in the sub-panel below each $P_c(s)$ plot. Vertical arrows on the slope subpanels indicate the maximum slope, which is used to infer the average size of cohesin extruded loops; this analysis indicates that the average extruded loop size is approximately 60-70 kbin control zygotes, and increases in the $Wapl^{\Delta}$ condition to over 120 kb. Horizontal arrows on the slope panels indicate the minimum slope, which can indicate cohesin linear density on the chromatin; notably, neither maternal or paternal $Scc1^{\Delta}$ zygotes have a minimum slope suggesting very low cohesin density, whereas minima exist in both control and $Wapl^{\Delta}$ conditions. Data is based on n($Wapl^{fl}$, maternal)= 7, n($Wapl^{fl}$, paternal)= 6, n($Wapl^{\Delta}$, maternal)= 8, n($Wapl^{\Delta}$, paternal)= 7, n($Scc1^{fl}$, maternal)= 13, n($Scc1^{fl}$, paternal)= 17, n($Scc1^{\Delta}$)= 28, n($Scc1^{\Delta}$)= 17 nuclei, from at least two independent experiments using 2-3 females per genotype each.

D-F. Simulated chromatin $P_c(s)$ for the control, $Scc1^{\Delta}$, and $Wapl^{\Delta}$ conditions. Simulation $P_c(s)$ curves shown in thick lines and experimental $P_c(s)$ curves in thin lines.

G-I. Representative images of the simulated paternal chromatin fiber used for the $P_c(s)$ calculations in Panels D-E. The chromatin fiber is coloured in gray, and the locations of the cohesins coloured in orange.

Figure 5: Live-cell imaging of vermicelli formation in wildtype and *Scc1$^{\Delta}$Wapl$^{\Delta}$* zygotes expressing Scc1-EGFP and H2B-mCherry

A. Germinal vesicle-stage oocytes were injected with mRNA encoding H2B-mCherry to mark chromosomes (magenta) and Scc1-EGFP to label cohesin (green), matured to meiosis II, fertilized *in vitro* and followed by time-lapse microscopy.

B. Still images of live wild-type zygotes expressing Scc1-EGFP and H2B-mCherry (n=4 zygotes, from one experiment using two females). Top row: Z-stack maximum intensity projection of zygotes. Middle and bottom row: Z-slices of the cropped areas (top left) showing paternal and maternal nuclei separately. Images were adjusted in brightness/contrast in individual imaging channels in the same manner for z-stacks and for the single z-slices. Scale bar: 10 µm. Hours after start of IVF are given.

C. Still images of live *Scc1$^{\Delta}$Wapl$^{\Delta}$* zygotes expressing Scc1-EGFP and H2B-mCherry (n=3 zygotes, from one experiment using two females). Top row: Z-stack maximum intensity projection of zygotes. Middle and bottom row: Z-slices of the cropped areas (top left) showing paternal and maternal nuclei separately. Arrows indicate Scc1-EGFP enriched structures. Images were adjusted in brightness/contrast in individual imaging channels in the same manner for z-stacks and for the single z-slices. Scale bar: 10 µm. Hours after start of IVF are given.

   Note: Experiments shown in B), C) were performed individually, but under the same conditions using the same mRNA injection mix.

Figure 6: Distinct maternal and paternal chromatin compaction in *Wapl$^{\Delta}$* zygotes

A. Representative images of paternal and maternal nuclei stained with DAPI of *Wapl^{fl}* (n=15) and *Wapl$^{\Delta}$* (n=33) zygotes (from two independent experiments using 2 females per genotype, see also Supplementary Figure 5). Top: *Wapl^{fl}*, Bottom: *Wapl$^{\Delta}$*. Left: Cropped z-slices from the middle section of the nucleus in fire look-up table. Middle: Cropped z-slices of nuclei separated by 3 µm. Right: Maximum Intensity Projection (MIP) of zygotes. Settings were adjusted for z-slices and MIP individually but in the same manner for *Wapl^{fl}* and *Wapl$^{\Delta}$* zygotes. Images were adjusted in brightness/contrast in the individual imaging channels using ImageJ. Scale bar: 10 µm.

B. MIP of zygotes seen in A) with blue ramp look up table to visualize difference in maternal and paternal vermicelli formation around prenucleolar bodies. Arrows indicate additional DAPI-intense structures in maternal zygotic nuclei. Images were adjusted in brightness/contrast in the individual imaging channels using ImageJ. Scale bar: 10 µm.

C. Coefficient of variation of DAPI intensity for nuclei of *Wapl^{fl}* (n=15) and *Wapl$^{\Delta}$* (n=21) zygotes (p-value=$1.88*10^{-7}$).

D. Boxplots showing Gray-Level Co-Occurrence Matrix (GLCM) contrast (local variation of intensity) in paternal (gray) and maternal (white) nuclei in *Wapl^{fl}* (n=15) and *Wapl$^{\Delta}$* (n=13) zygotes with increasing window sizes. Two outliers (maternal *Wapl$^{\Delta}$* window 8) with values 3242.7 and 4037.4 are not shown.

E. Boxplots showing size of detected bright objects (voxels) inside paternal (grey) and maternal (white) nuclei in Waplfl (n=15) and WaplΔ (n=21) zygotes; note the log scale on y axis.

Figure 7: The influence of cohesin on inter-chromosomal contacts.

A. The number of snHi-C contacts mapping to regions on distinct chromosomes, as a fraction of the total number of mapped contacts is shown for each of the experimental conditions. Error bars are the standard error of the mean. The distribution of values from individual nuclei is shown in blue. (n(*Wapl*^{fl}, maternal)= 7, n(*Wapl*^{fl}, paternal)= 6, n(*Wapl*$^{\Delta}$, maternal)= 8, n(*Wapl*$^{\Delta}$, paternal)= 7, n(*Scc1*^{fl}, maternal)= 13, n(*Scc1*^{fl}, paternal)= 17, n(*Scc1*$^{\Delta}$)= 28, n(*Scc1*$^{\Delta}$)= 17 nuclei, data is based on at least two independent experiments using 2-3 females per genotype each)

B. Spatial, geometric properties of simulated chromatin undergoing loop extrusion for different loop extrusion parameters. The fraction of inter-chromosomal contacts were calculated using a Hi-C cutoff radius of 5 monomers (75 nm). The surface area and volume of the simulated chromatin fiber were calculated from the concave hull, and used an effective radius for each monomer equal to the Hi-C cutoff radius (see **Material and Methods**).

C. A schematic model illustrating that cohesin loop extrusion can modulate the surface area smoothness of chromosomes and reduce the frequency of inter-chromosomal interactions.

Figure 8: The effect of loop extrusion on the simulated chromatin surface area, volume, and inter-chromosomal interactions

A. Representative polymer conformations of simulated chromatin undergoing loop extrusion. The rendered surface is the alpha shape (concave hull polygon) created using spheres centered on chromosome monomers. The monomers have radius 75 nm, which were chosen to be equal to the simulated Hi-C capture frequency. With increasing cohesin density and processivity, the chromosome compacts and becomes more linearly ordered and the concave hull surface becomes “smoother”.

B. Volume, surface area, and the fraction of inter-chromosomal contacts are shown as a function of loop extrusion simulation parameters. Values reported are the averages and standard deviations for each parameter. Averages were computed from 3 randomly sampled simulation conformations and over all possible simulation parameters tested (See **Materials and Methods**)

EXPANDED VIEW FIGURE LEGENDS

Expanded View Figure 1: Average TADs called in many cell types show enrichments in zygote Hi-C and snHi-C

A. TAD boundaries were *de novo* identified in many cell types and Hi-C data sets using the corner score as described in Schwarzer et al., 2017. The *de novo* identified boundaries were used to generate average TAD profiles (shown in B), and the TAD strength was computed (see **Materials and Methods**). Notably, all data sets showed enrichments for TADs for all identified boundaries except MII oocytes (Du et al., 2017) which are in mitosis and are not expected to have TADs (Naumova et al., 2013), and our $Scc1^{\Delta}$ zygotes.

B. Average TAD profiles in different data sets are shown called from boundaries identified in mouse ES cells (Nora et al., 2017) using the corner score as in Schwarzer et al., 2017. These average TAD profiles were used to calculate the TAD strengths in (A) for the top row of the matrix.

Expanded View Figure 2: TAD-like structures can be directly seen in zygote population Hi-C

A. An example region on chromosome 2 is shown for zygotic, 2-cell and 8-cell embryos illustrating that in bulk Hi-C data (Du et al., 2017; Ke et al., 2017) it is possible to identify enrichments of contacts resembling TADs and loops. Vertical lines are drawn to guide the eye and compare the locations of boundaries visually identified in the Du et al. 8-cell data. RefSeq gene annotation from the UCSC Genome browser is shown below.

B. Same as panel (A) but for an example region on chromosome 5.

Expanded View Figure 3: Additional information on conditional knockouts

A. Loop strengths were calculated using the three 60 x 60 kb square regions shown. The average value within the middle box (black) was divided by the average of the combined top left and bottom right (green) boxes. The resulting number was subtracted by 1 to indicate the fractional increase in loop strength above the background.

B. Immunofluorescence staining of Scc1 in *in situ* fixed $Scc1^{fl}$ (n=11) and $Scc1^{\Delta}$ zygotes (n=12, from one experiment using 2 females of each genotype). DNA in magenta, Scc1 in grey/green. Images were adjusted in brightness/contrast in the individual channels using ImageJ. Scale bar: 10µm. Left: Single z-slice of zygotes. Right: Single z-slice of the maximum cross-section area of maternal and paternal nuclei. Cropped area is indicated.

C. Loops, TADs, and compartment saddle plots for the $Scc1^{fl}$, $Wapl^{fl}$, $Scc1^{\Delta}$ and $Wapl^{\Delta}$ conditions shown separately for the maternal and paternal data. The average strength of each feature is indicated in each panel. Data shown are based on n($Wapl^{fl}$, maternal)= 7, n($Wapl^{fl}$, paternal)= 6, n($Wapl^{\Delta}$, maternal)= 8, n($Wapl^{\Delta}$, paternal)= 7, n($Scc1^{fl}$, maternal)= 13, n($Scc1^{fl}$, paternal)= 17, n($Scc1^{\Delta}$)= 28, n($Scc1^{\Delta}$)= 17 nuclei, from at least two independent experiments using two to three females per genotype each.

D. Insulation scores calculated with a sliding diamond of size 40 kb, with the "zero" position denoting a domain boundary identified previously in CH12-LX cells (Rao et. al, 2014). Distances are reported in base-pairs from a domain boundary. The average over all domain boundaries is reported; error bars are the standard error on the mean insulation score.

Expanded View Figure 4: Genome-wide contact probability, $P_c(s)$, for chromatin loci separated by genomic distances, s, underlying maternal *Wapl*$^{\Delta}$ simulation

A. Slopes of $P_c(s)$ curves as a function of genomic separation for N=30000 polymer models with loop extrusion. The rows show different loop extrusion processivities (proc), and columns show different linear separations (sep) between cohesins; the latter is related to the number of cohesins via the relation: separations = (chromosome length) / (number of bound cohesins). The vertical line on each plot indicates the average extruded loop length. All $P_c(s)$ plots in the left 6 rows/columns were calculated for a Hi-C contact radius of 5 monomers (75 nm). Plots on the right are a subset of plots on the left, for contact radius of 2 monomers (30 nm), and 10 monomers (150 nm), indicating that the inferred average extruded loop length does not vary significantly with the choice of Hi-C capture radius. Note that average extruded loop length is different from processivity, especially in a dense regime where processivity is greater than separation; due to stalling of cohesins when encountering each other and at simulated TAD boundaries, the average loop length then becomes less than processivity; see Goloborodko et al., 2016 for details.

B. The analysis of the slope of $\log(P_c(s))$ applied on recently published *Wapl*$^{\Delta}$ Hi-C data (see Haarhuis et al., 2017). Consistently with experimental FRAP data (Haarhuis et al., 2017), we find that in *Wapl*$^{\Delta}$ conditions the processivity, which is linearly related to the chromatin-bound lifetime of cohesin, is increased >2 above control conditions. Similarly, we find that the numbers of bound cohesins is >1 but less than 2-fold enriched above controls in *Wapl*$^{\Delta}$; this is consistent with quantitative immunofluorescence data, showing a 1.5-fold enrichment for cohesins in *Wapl*$^{\Delta}$ versus controls (Haarhuis et al., 2017).

C. A representative image of the maternal *Wapl*$^{\Delta}$ simulation. The chromatin fiber is coloured in gray, and the locations of the cohesins coloured in orange, indicating that some cohesin vermicelli is visibly formed.

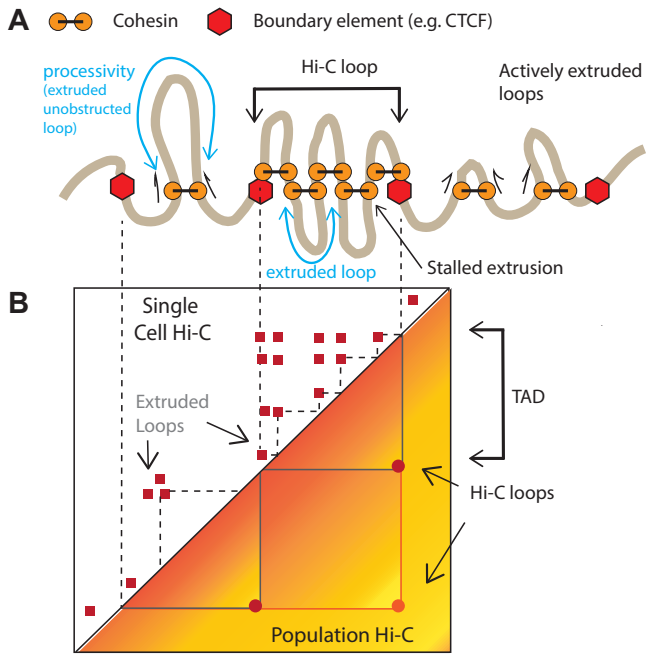
A
Cohesin
Boundary element (e.g. CTCF)
processivity
(extruded
unobstructed
loop)
Hi-C loop
Actively extruded
loops
extruded loop
Stalled extrusion
B
Single
Cell Hi-C
Extruded
Loops
TAD
Hi-C loops
Population Hi-C

Figure 1

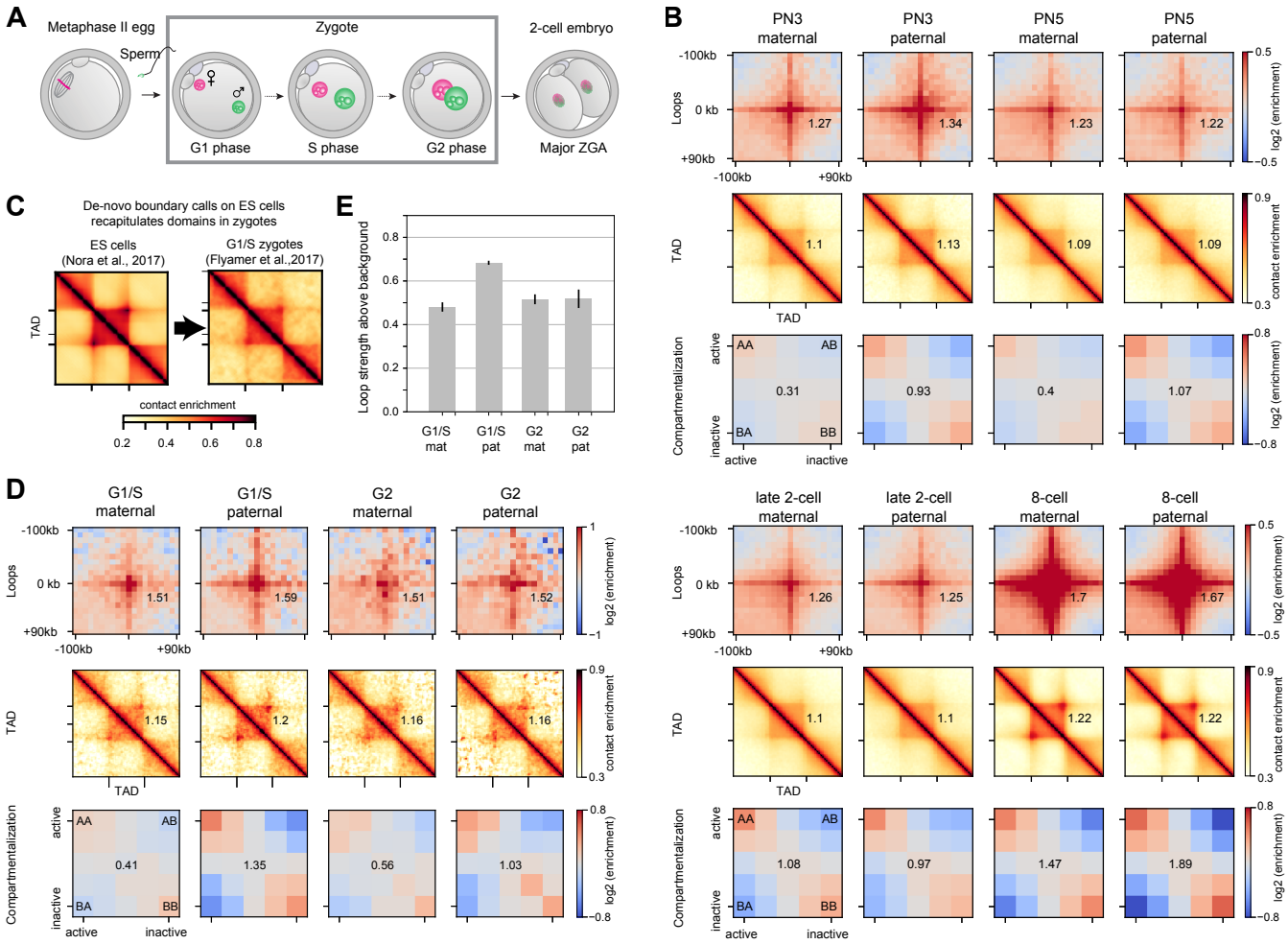
A
Metaphase II egg
Sperm
Zygote
2-cell embryo
G1 phase
S phase
G2 phase
Major ZGA
B
PN3 maternal
PN3 paternal
PN5 maternal
PN5 paternal
Loops
TAD
Compartmentalization
contact enrichment
log2 (enrichment)
late 2-cell maternal
late 2-cell paternal
8-cell maternal
8-cell paternal
C
De-novo boundary calls on ES cells recapitulates domains in zygotes
ES cells (Nora et al., 2017)
G1/S zygotes (Flyamer et al.,2017)
D
G1/S maternal
G1/S paternal
G2 maternal
G2 paternal
E
Loop strength above background
G1/S mat
G1/S pat
G2 mat
G2 pat

Figure 2

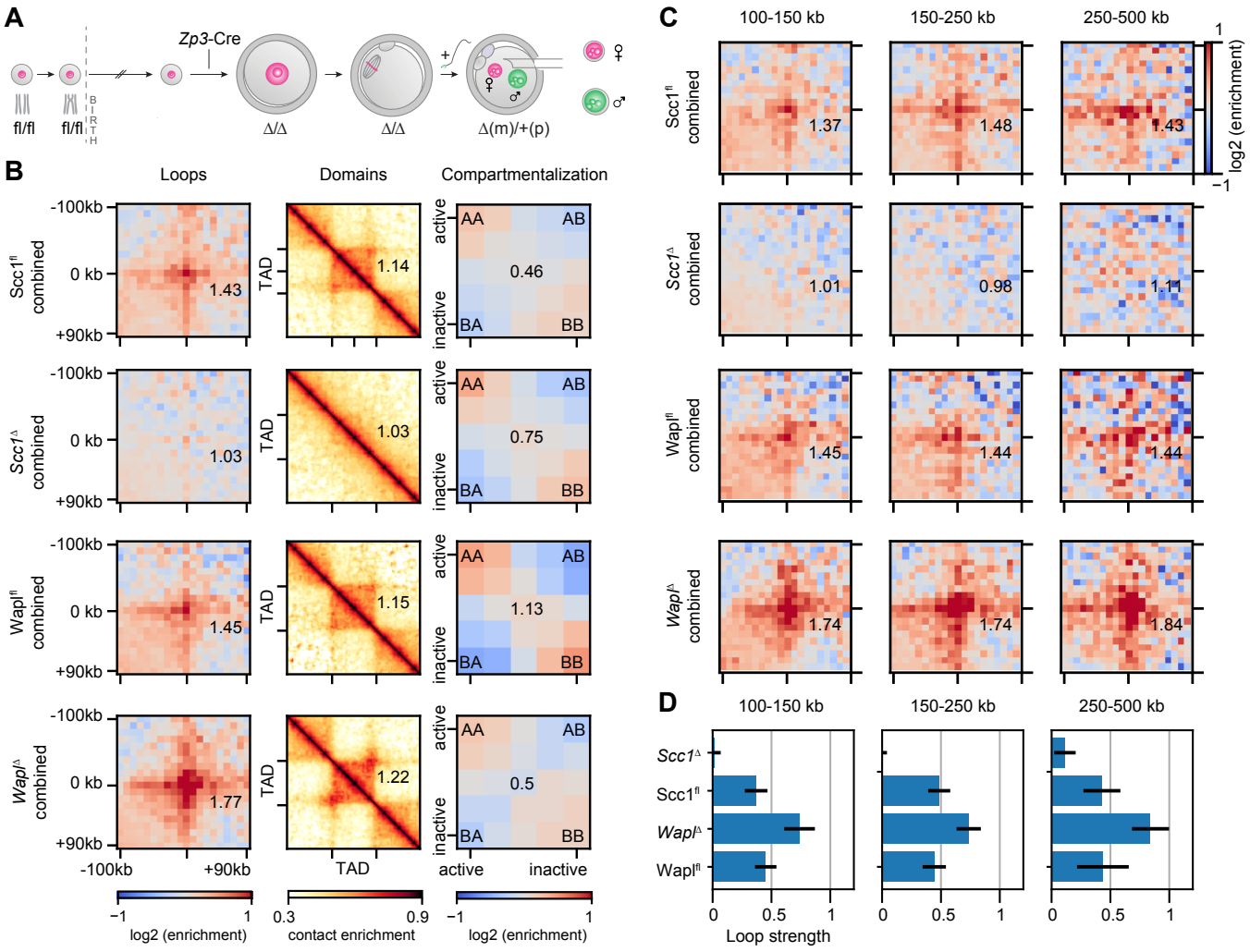
A
Zp3-Cre
fl/fl
fl/fl
BIRTH
Δ/Δ
Δ/Δ
Δ(m)/+(p)
B
Loops
Domains
Compartmentalization
Scc1fl combined
Scc1Δ combined
Waplfl combined
WaplΔ combined
-100kb
0 kb
+90kb
1.43
1.03
1.45
1.77
TAD
1.14
1.03
1.15
1.22
active
inactive
AA
AB
BA
BB
0.46
0.75
1.13
0.5
log2 (enrichment)
contact enrichment
C
100-150 kb
150-250 kb
250-500 kb
1.37
1.48
1.43
1.01
0.98
1.11
1.45
1.44
1.44
1.74
1.74
1.84
log2 (enrichment)
D
Scc1Δ
Scc1fl
WaplΔ
Waplfl
Loop strength

Figure 3

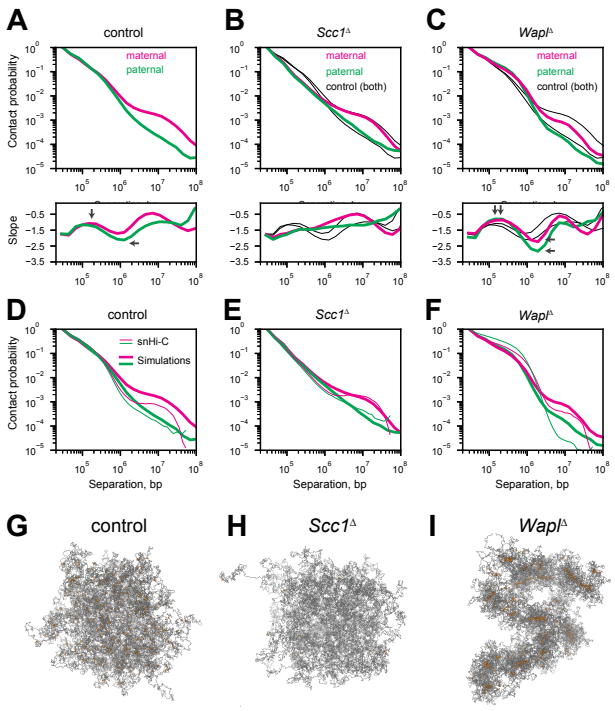
A
control
B
Scc1Δ
C
WaplΔ
maternal
paternal
control (both)
Contact probability
Slope
D
control
E
Scc1Δ
F
WaplΔ
snHi-C
Simulations
Separation, bp
G
control
H
Scc1Δ
I
WaplΔ

Figure 4

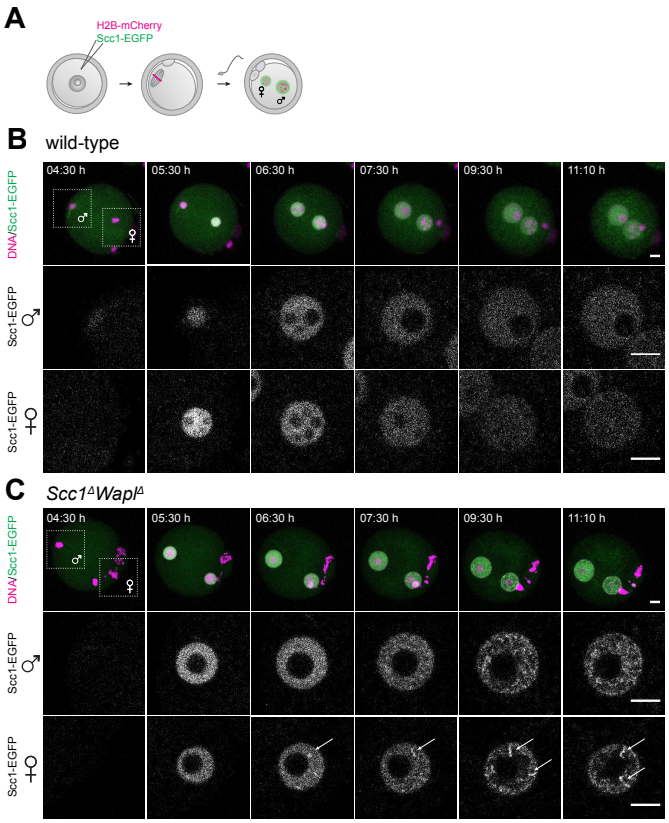
A
H2B-mCherry
Scc1-EGFP
B
wild-type
04:30 h
05:30 h
06:30 h
07:30 h
09:30 h
11:10 h
DNA/Scc1-EGFP
Scc1-EGFP ♂
Scc1-EGFP ♀
C
Scc1^Δ Wapl^Δ
04:30 h
05:30 h
06:30 h
07:30 h
09:30 h
11:10 h
DNA/Scc1-EGFP
Scc1-EGFP ♂
Scc1-EGFP ♀

Figure 5

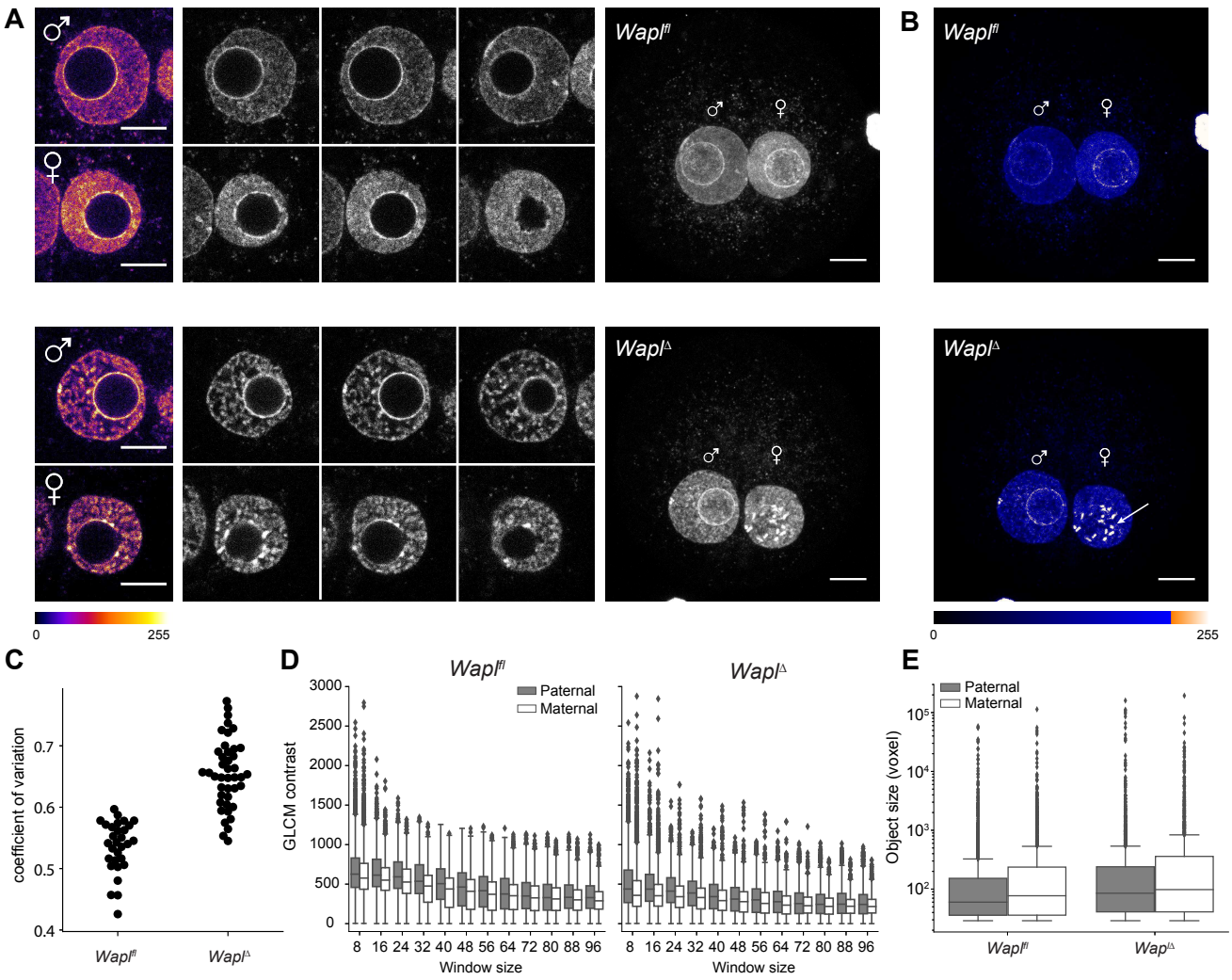
A
B
Wapl^fl
Wapl^Δ
♂
♀
0
255
C
coefficient of variation
0.7
0.6
0.5
0.4
Wapl^fl
Wapl^Δ
D
Wapl^fl
Wapl^Δ
Paternal
Maternal
GLCM contrast
3000
2500
2000
1500
1000
500
0
8 16 24 32 40 48 56 64 72 80 88 96
Window size
E
Paternal
Maternal
Object size (voxel)
10^5
10^4
10^3
10^2
Wapl^fl
Wapl^Δ

Figure 6

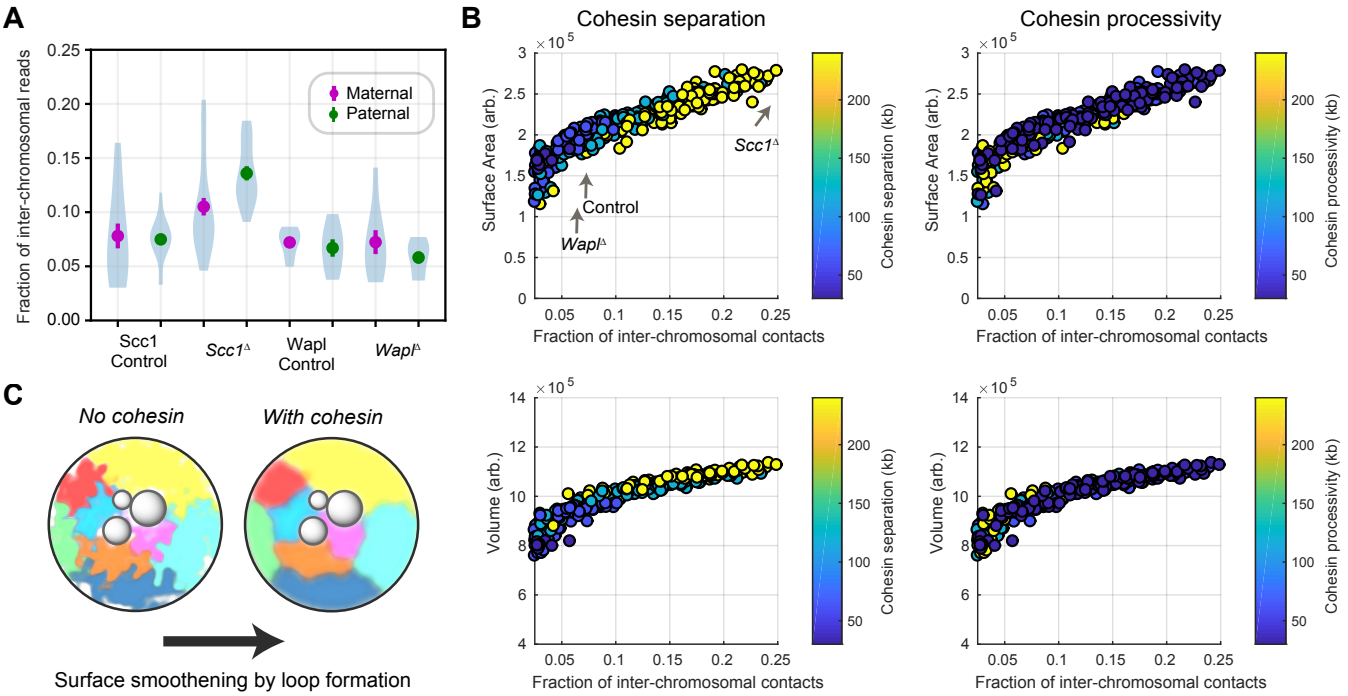
A
Fraction of inter-chromosomal reads
Maternal
Paternal
Scc1 Control
Scc1Δ
Wapl Control
WaplΔ
B
Cohesin separation
Cohesin processivity
Surface Area (arb.)
Volume (arb.)
Fraction of inter-chromosomal contacts
Cohesin separation (kb)
Cohesin processivity (kb)
Scc1Δ
Control
WaplΔ
C
No cohesin
With cohesin
Surface smoothening by loop formation

Figure 7

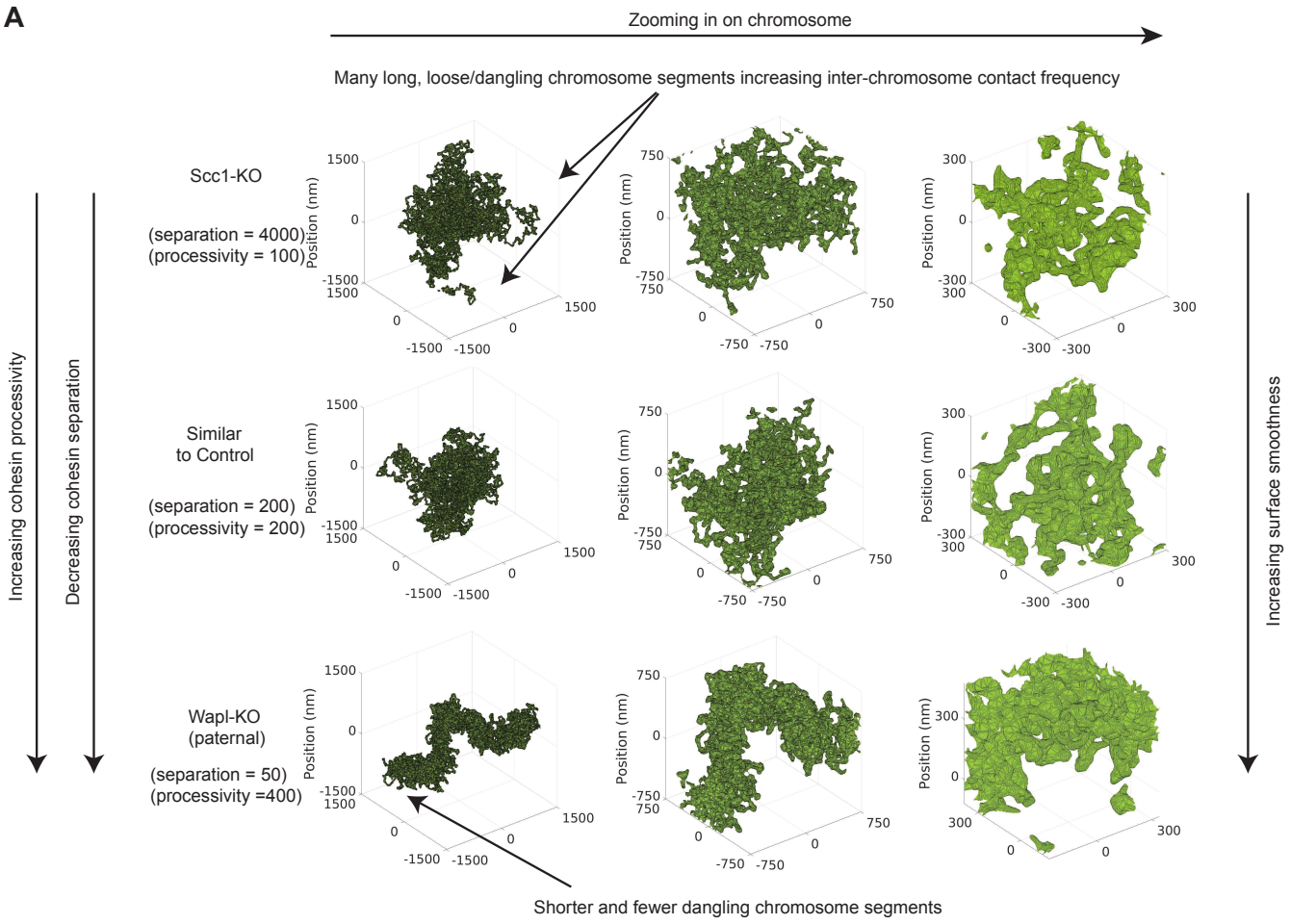
A
Zooming in on chromosome
Many long, loose/dangling chromosome segments increasing inter-chromosome contact frequency
Scc1-KO
(separation = 4000)
(processivity = 100)
Similar
to Control
(separation = 200)
(processivity = 200)
Wapl-KO
(paternal)
(separation = 50)
(processivity =400)
Position (nm)
Increasing cohesin processivity
Decreasing cohesin separation
Increasing surface smoothness
Shorter and fewer dangling chromosome segments

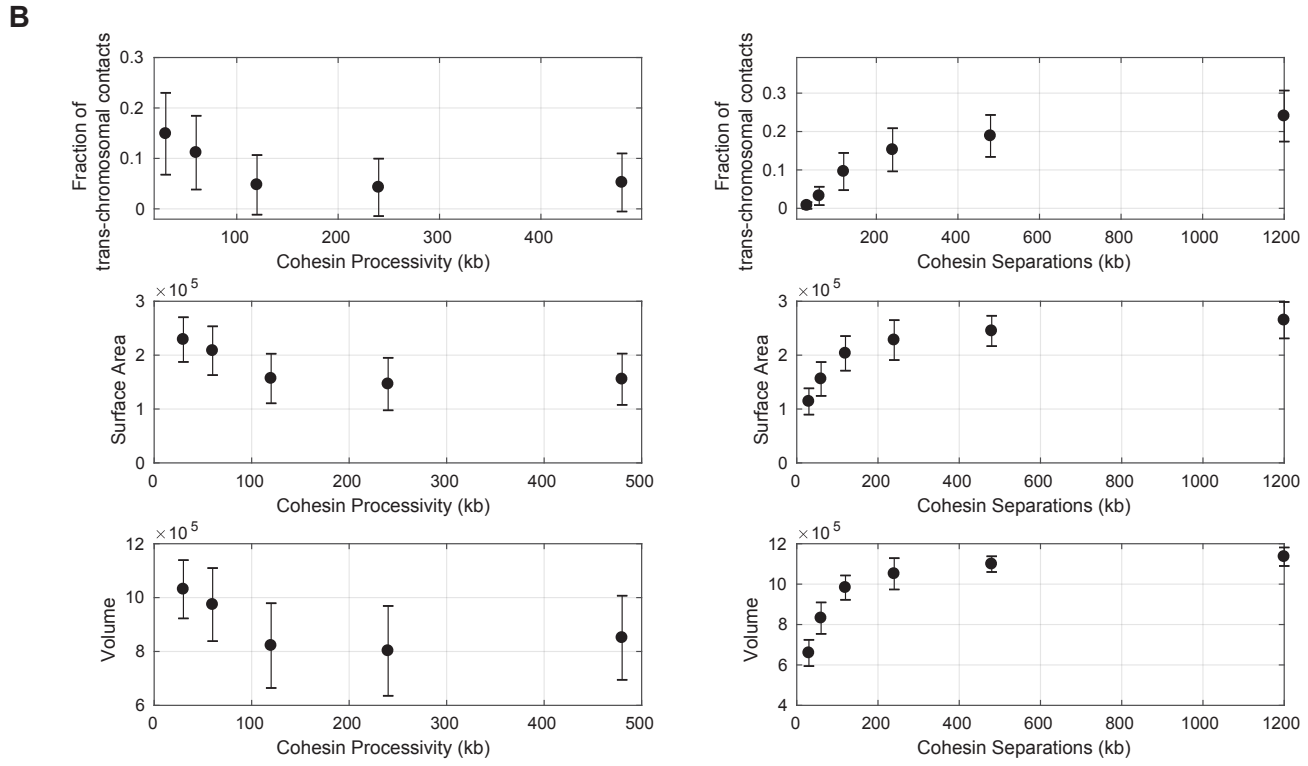
B
Fraction of trans-chromosomal contacts
Surface Area
Volume
Cohesin Processivity (kb)
Cohesin Separations (kb)

Figure 8


A
Data set used to calculate the TAD strength using the de novo identified boundaries
Data set used to de novo identify domain boundaries
Nora et al., 2017_ES cells
Rao et al., 2014_CH12-LX
Selvaraj et al., 2013_ES cells F123
Dixon et al., 2012_ES cells
Dixon et al., 2012_Mouse Cortex
Sofueva et al., 2013_Astrocytes
Sofueva et al., 2013_Neural Stem Cells
Zhang et al., 2012_ProB
Ke et al., 2017_8-cell
Du et al., 2017_8-cell
Du et al., 2017_2-cell_late
Du et al., 2017_sperm
Ke et al., 2017_sperm
Schwarzer et al., 2017_WT
Ke et al., 2017_zygote
Du et al., 2017_PN3 zygote
Du et al., 2017_MII-oocyte
2.0
1.8
1.6
1.4
1.2
1.0
TAD strength
Nora et al., 2017_ES cells
Rao et al., 2014_CH12-LX
Selvaraj et al., 2013_ES cells F123
Dixon et al., 2012_ES cells
Dixon et al., 2012_Mouse Cortex
Sofueva et al., 2013_Astrocytes
Sofueva et al., 2013_Neural Stem Cells
Zhang et al., 2012_ProB
Ke et al., 2017_8-cell
Du et al., 2017_8-cell
Du et al., 2017_2-cell_late
Du et al., 2017_sperm
Ke et al., 2017_sperm
Schwarzer et al., 2017_WT
Ke et al., 2017_zygote
Du et al., 2017_PN3 zygote
Du et al., 2017_MII-oocyte
Du et al., 2017_PN5 zygote
Nora et al., 2017_CTCFΔ
Ke et al., 2017_E3.5
Lin et al., 2012_proB
Lin et al., 2012_preproB
Zhang et al., 2012_proB
Schwarzer et al.,2017_Nipbl
Scc1fl+Waplfl
WaplΔ
Scc1Δ
G2
Flyamer et al., 2017_G1/S
snHi-C

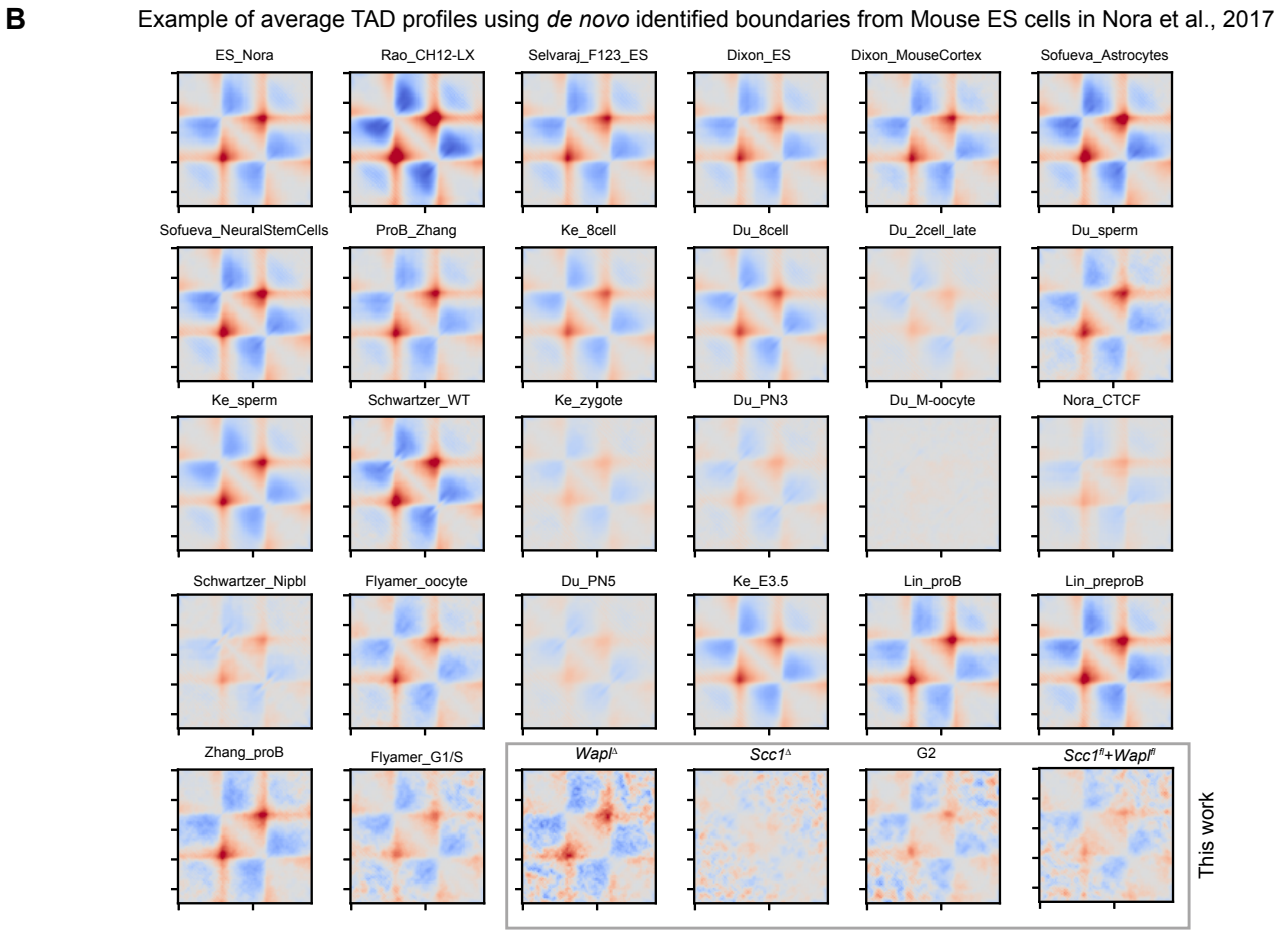
B
Example of average TAD profiles using de novo identified boundaries from Mouse ES cells in Nora et al., 2017
ES_Nora
Rao_CH12-LX
Selvaraj_F123_ES
Dixon_ES
Dixon_MouseCortex
Sofueva_Astrocytes
Sofueva_NeuralStemCells
ProB_Zhang
Ke_8cell
Du_8cell
Du_2cell_late
Du_sperm
Ke_sperm
Schwartzer_WT
Ke_zygote
Du_PN3
Du_M-oocyte
Nora_CTCF
Schwartzer_Nipbl
Flyamer_oocyte
Du_PN5
Ke_E3.5
Lin_proB
Lin_preproB
Zhang_proB
Flyamer_G1/S
WaplΔ
Scc1Δ
G2
Scc1fl+Waplfl
This work

Figure EV1

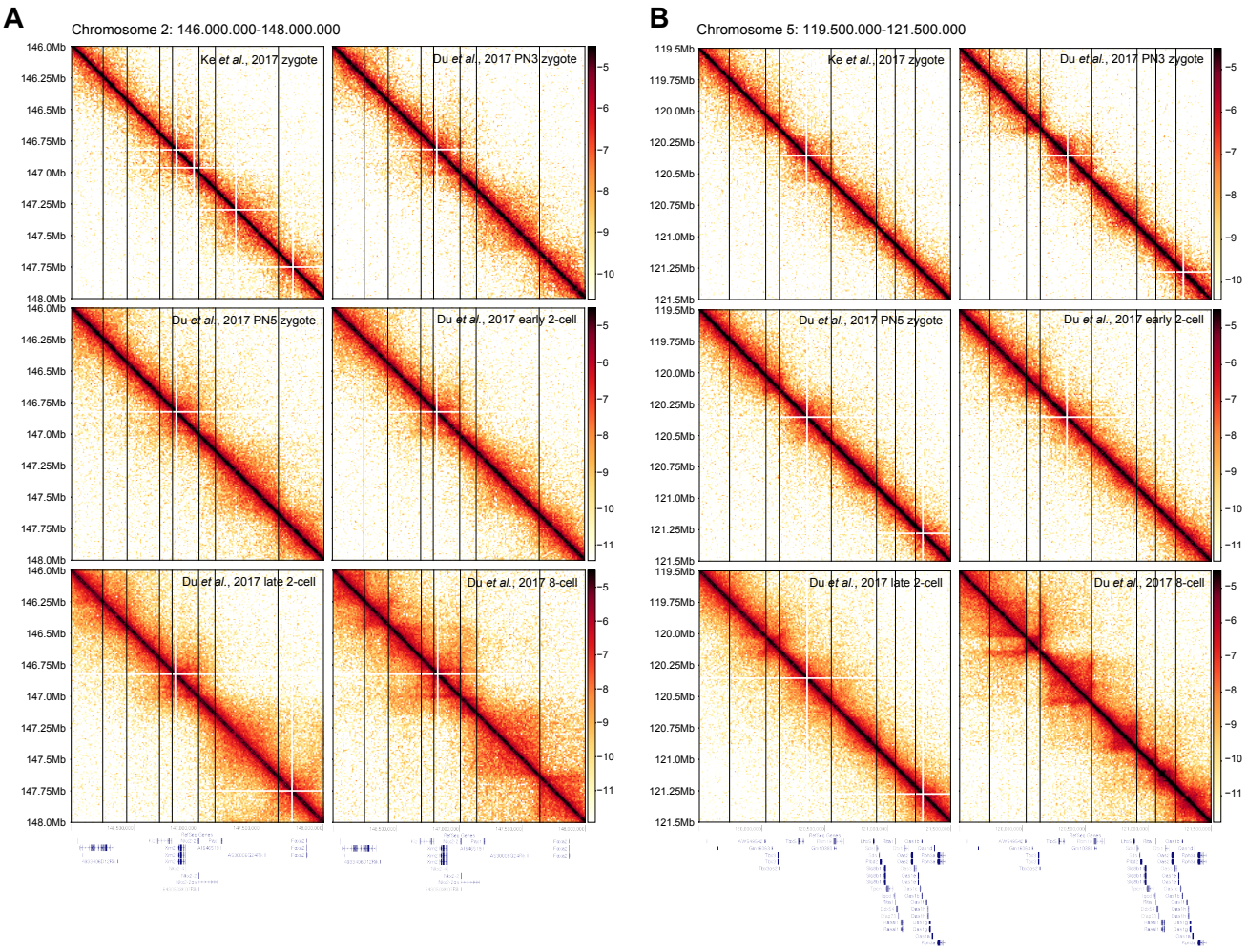
A
Chromosome 2: 146.000.000-148.000.000
Ke et al., 2017 zygote
Du et al., 2017 PN3 zygote
Du et al., 2017 PN5 zygote
Du et al., 2017 early 2-cell
Du et al., 2017 late 2-cell
Du et al., 2017 8-cell
B
Chromosome 5: 119.500.000-121.500.000
Ke et al., 2017 zygote
Du et al., 2017 PN3 zygote
Du et al., 2017 PN5 zygote
Du et al., 2017 early 2-cell
Du et al., 2017 late 2-cell
Du et al., 2017 8-cell

Figure EV2

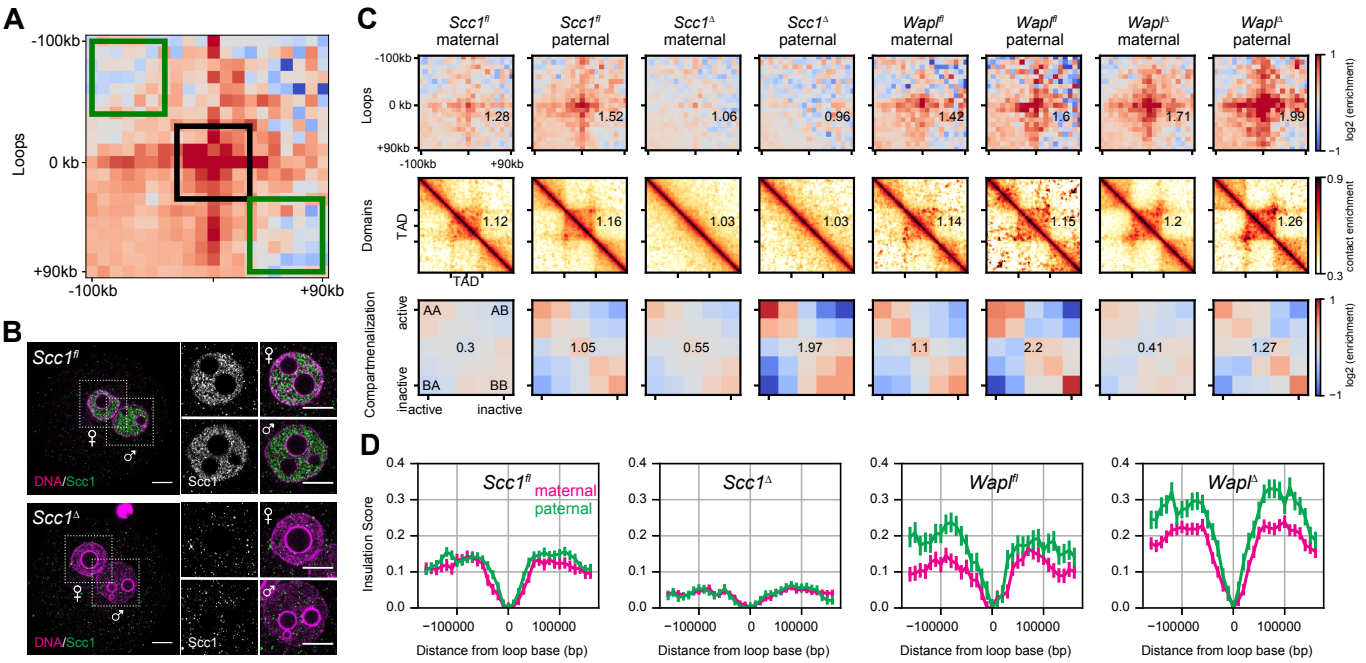
A
-100kb
0 kb
+90kb
Loops
-100kb
+90kb
B
Scc1fl
DNA/Scc1
Scc1
Scc1Δ
C
Scc1fl maternal
Scc1fl paternal
Scc1Δ maternal
Scc1Δ paternal
Waplfl maternal
Waplfl paternal
WaplΔ maternal
WaplΔ paternal
Loops
Domains
TAD
Compartmentalization
active
inactive
AA
AB
BA
BB
log2 (enrichment)
contact enrichment
D
Insulation Score
maternal
paternal
Distance from loop base (bp)

Figure EV3

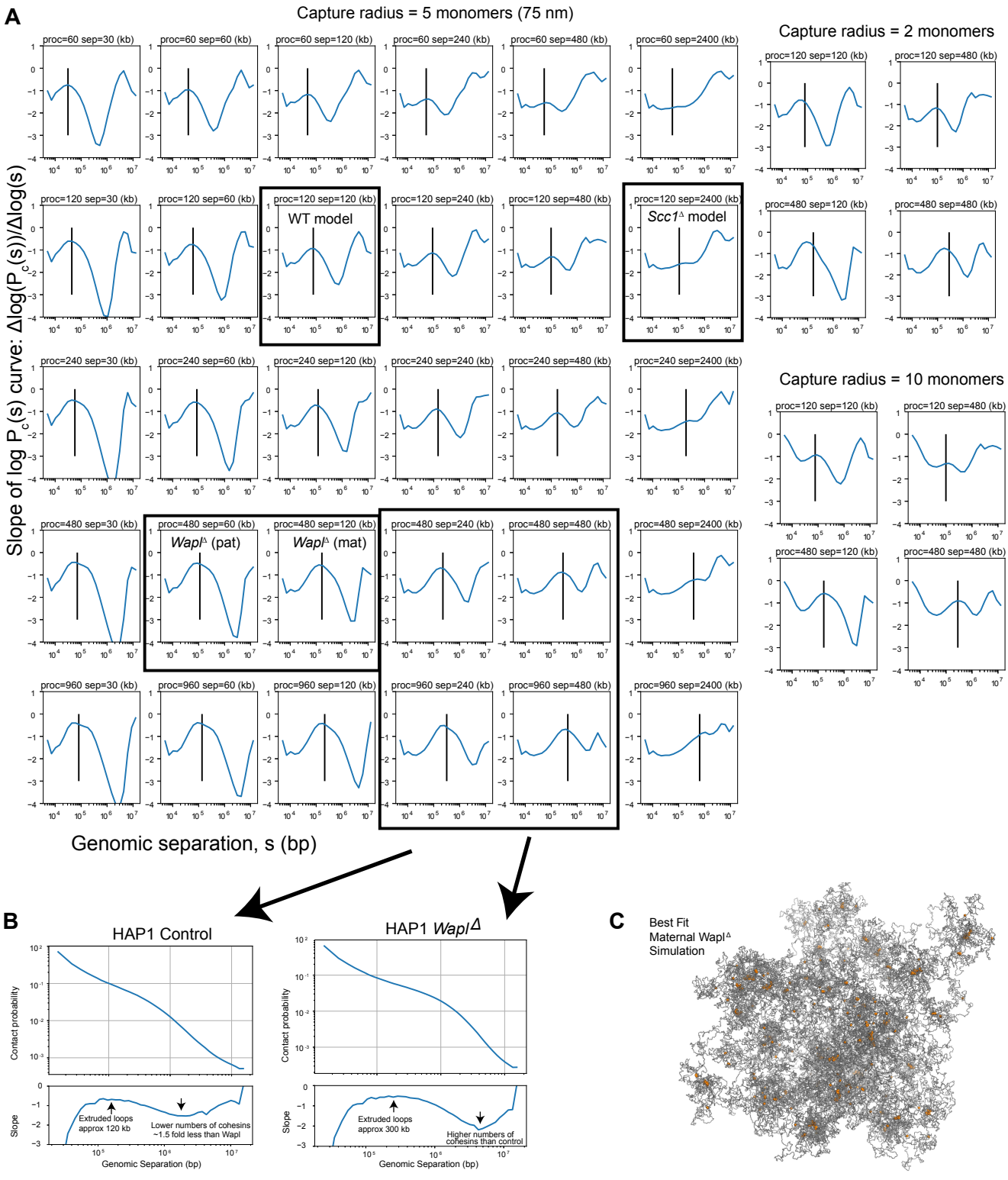
A
Capture radius = 5 monomers (75 nm)
Capture radius = 2 monomers
Capture radius = 10 monomers
WT model
Scc1Δ model
WaplΔ (pat)
WaplΔ (mat)
Slope of log Pc(s) curve: Δlog(Pc(s))/Δlog(s)
Genomic separation, s (bp)
B
HAP1 Control
HAP1 WaplΔ
Contact probability
Slope
Extruded loops approx 120 kb
Lower numbers of cohesins ~1.5 fold less than Wapl
Extruded loops approx 300 kb
Higher numbers of cohesins than control
Genomic Separation (bp)
C
Best Fit
Maternal WaplΔ
Simulation

Figure EV4